



Constraints on the stress state of the San Andreas Fault with analysis based on core and cuttings from San Andreas Fault Observatory at Depth (SAFOD) drilling phases 1 and 2

Sheryl Tembe,¹ David Lockner,² and Teng-fong Wong³

Received 17 June 2008; revised 18 June 2009; accepted 24 July 2009; published 5 November 2009.

[1] Analysis of field data has led different investigators to conclude that the San Andreas Fault (SAF) has either anomalously low frictional sliding strength ($\mu < 0.2$) or strength consistent with standard laboratory tests ($\mu > 0.6$). Arguments for the apparent weakness of the SAF generally hinge on conceptual models involving intrinsically weak gouge or elevated pore pressure within the fault zone. Some models assert that weak gouge and/or high pore pressure exist under static conditions while others consider strength loss or fluid pressure increase due to rapid coseismic fault slip. The present paper is composed of three parts. First, we develop generalized equations, based on and consistent with the Rice (1992) fault zone model to relate stress orientation and magnitude to depth-dependent coefficient of friction and pore pressure. Second, we present temperature- and pressure-dependent friction measurements from wet illite-rich fault gouge extracted from San Andreas Fault Observatory at Depth (SAFOD) phase 1 core samples and from weak minerals associated with the San Andreas Fault. Third, we reevaluate the state of stress on the San Andreas Fault in light of new constraints imposed by SAFOD borehole data. Pure talc ($\mu \approx 0.1$) had the lowest strength considered and was sufficiently weak to satisfy weak fault heat flow and stress orientation constraints with hydrostatic pore pressure. Other fault gouges showed a systematic increase in strength with increasing temperature and pressure. In this case, heat flow and stress orientation constraints would require elevated pore pressure and, in some cases, fault zone pore pressure in excess of vertical stress.

Citation: Tembe, S., D. Lockner, and T.-f. Wong (2009), Constraints on the stress state of the San Andreas Fault with analysis based on core and cuttings from San Andreas Fault Observatory at Depth (SAFOD) drilling phases 1 and 2, *J. Geophys. Res.*, *114*, B11401, doi:10.1029/2008JB005883.

1. Introduction

[2] A multiplicity of geophysical and geological observations have indicated that the San Andreas Fault (SAF) is mechanically weak. Absence of an appreciable heat flow anomaly near the fault trace constrains the shear stress averaged over the upper 14 km of the SAF to be less than about 20 MPa [e.g., *Brune et al.*, 1969; *Lachenbruch and Sass*, 1980, 1992]. Seismological and geological indicators constrain the maximum principal stress to be at a high angle to the strike of the SAF [e.g., *Mount and Suppe*, 1987; *Zoback et al.*, 1987]. Together with related measurements of the stress magnitude, such data imply that not only is the SAF weak in an absolute sense, it is also weak when compared to the surrounding crust [*Zoback et al.*, 1987; *Hickman and Zoback*, 2004]. More recently, *Scholz* [2000]

and *Scholz and Hanks* [2004] have argued that Southern California data are consistent with a strong SAF model. *Hardebeck and Michael* [2004] have reviewed available data for both northern and southern California, especially focal mechanism inversions and concluded that an intermediate strength SAF, rather than either of the end-member strong or weak fault models, is indicated. It is possible that stress orientations adjacent to locked portions of the SAF are consistent with high fault strength while stresses at the San Andreas Fault Observatory at Depth (SAFOD) site, located at the transition from locked to creeping portions of the fault near Parkfield, California, are more consistent with low fault strength. Our analysis will not resolve this debate that has continued for four decades. Instead, we provide new strength data from fault gouge obtained at depth in the SAFOD drill hole near the active trace of the SAF and consider the trade-offs between stress orientation, fluid pressure and fault strength that can satisfy various observational constraints.

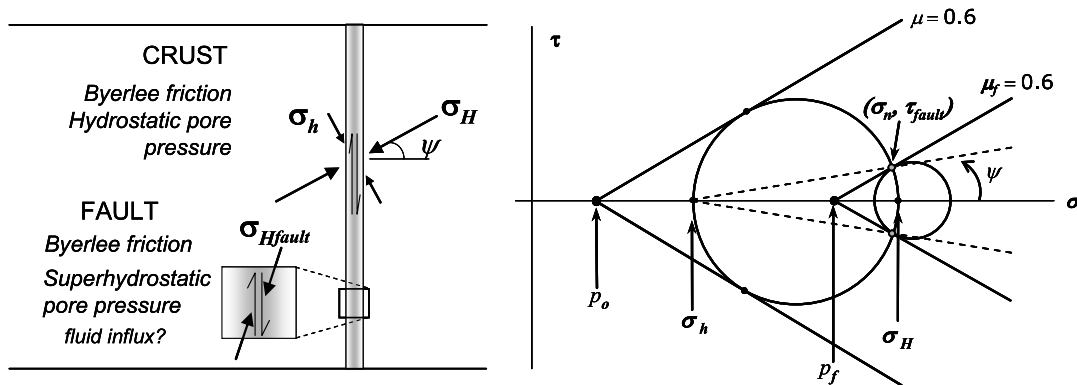
[3] If the SAF is strong and large earthquakes dissipate energy primarily through heat generation in the fault and near-fault regions as argued by *Scholz* [2000], then there is little need to appeal to either static or transient elevated fluid

¹Institute for Soil Mechanics and Rock Mechanics, Karlsruhe Institute of Technology, Karlsruhe, Germany.

²U.S. Geological Survey, Menlo Park, California, USA.

³Department of Geosciences, State University of New York at Stony Brook, Stony Brook, New York, USA.

a. High Fault Zone Pore Pressure



b. Low Fault Zone Friction

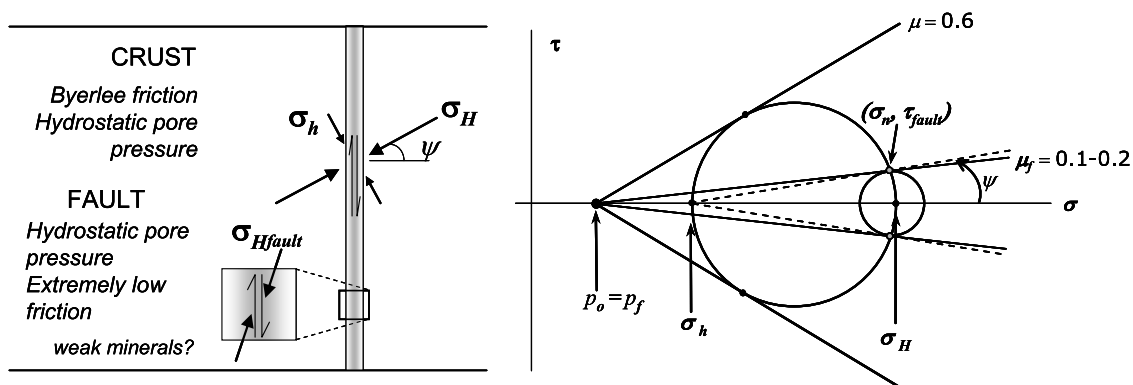


Figure 1. Mohr circle diagrams represent two conventional end-member models of fault weakening with differing stress states in the fault and country rock. In both models, a strike-slip faulting regime is imposed in the country rock (large circle) with Byerlee frictional strength μ . The fault zone stress state is represented by the small Mohr circle. The dashed line at angle ψ intersects the Mohr circle for the country rock at a point corresponding to the shear and normal stresses, which should be continuous across the interface between fault and country rock. The tangent that touches the small Mohr circle at this point is inclined at a slope corresponding to the friction coefficient μ_f of the fault zone. Weakening of the fault zone is possible if (1) elevated pore pressure can be generated and maintained in the fault zone, with identical frictional strengths in the fault and country rock ($\mu = \mu_f$) or (2) the fault zone under hydrostatic pore pressure is intrinsically weak due to the presence of weak minerals.

pressure. In this case, the analysis that we present indicates that near-hydrostatic fluid pressure can be expected in the fault. On the other hand, geophysical observations can be interpreted to suggest that the slip-parallel shear stress magnitude inferred for the SAF is significantly lower than that predicted by a fault model based on the *Anderson* [1951] theory of faulting and laboratory-derived rock friction data [Byerlee, 1978], assuming a hydrostatic pore pressure gradient [e.g., *Brace and Kohlstedt*, 1980]. Some of these observations come specifically from measurements at SAFOD and the surrounding region and will be the focus of much of this paper. If the laboratory strength data for fault rocks are correct, then one way to reconcile lab and field observations is to appeal to elevated pore fluid pressure within the fault zone. However, the necessary fluid pressures should not exceed the minimum compressive stress, to ensure that hydraulic fracturing does not occur in the host rock. This theoretical problem was overcome

independently by *Byerlee* [1990] and *Rice* [1992] when they recognized that for a mature fault such as the San Andreas, a pore pressure gradient could be established between the fault core and the surrounding host rock, such that the pore pressure would never exceed the local minimum principal stress. At the same time, pore pressure in the fault core could rise as needed, reducing the effective normal stress and therefore the fault strength. An end-member conceptual model of this type is shown in Figure 1a, where the adjoining crust is considered to be relatively strong, with limiting stresses comparable to those required to induce thrust faulting in a rock mass with Byerlee frictional strength [Brace and Kohlstedt, 1980] (see also, e.g., *Hardebeck and Michael* [2004, Figure 9]). A critical assumption in this scenario is that a pronounced pore pressure excess ($p_f > p_o$) can be generated and maintained within the fault gouge that would allow frictional sliding to occur at a low shear stress level, with a local stress state in the strike-slip regime and

maximum principal stress oriented almost normal to the fault plane (Figure 1a). Note that in this scenario, principal stresses in the gouge zone exceed the corresponding principal stresses in the host rock, but the high local pore pressure results in low effective pressures and low strength.

[4] In contrast, the vertical pore pressure gradient in the other end-member case (Figure 1b) is assumed to be hydrostatic ($p_f = p_o$). In the absence of pore pressure excess, this scenario is viable only if frictional strength of the fault gouge is intrinsically low, possibly due to the abundance of weak minerals such as smectite, illite, serpentine or talc with friction coefficients significantly lower than predicted by Byerlee's rule for crystalline rocks and framework silicates ($\mu = 0.6 - 0.85$). (We define coefficient of friction as the simple ratio of shear strength to effective normal stress: $\mu = \tau/(\sigma_n - p)$ with p = pore pressure.) *Rice* [1992] and *Byerlee* [1990] note that for a weak plastic (von Mises) fault gouge, deformation leads to principal stresses within the fault core that rotate to an angle of 45° to the fault. A similar result was obtained for Coulomb failure of granular material by *Byerlee and Savage* [1992]. One of the scientific objectives of SAFOD is to acquire pertinent borehole data and laboratory core data that would constrain the stress state and pore pressure of the SAF near Parkfield and determine which, if either, of these models applies to the fault.

[5] The SAFOD experiment included two boreholes. A pilot hole was drilled vertically in 2002. After passing through 760 m of Tertiary and Quaternary sedimentary rocks, it penetrated through Salinian granite basement to a depth of 2170 m, at a distance of 1.8 km southwest of the surface trace of the SAF. Heat flow and stress orientation in the SAFOD pilot hole are in basic agreement with previous regional data for the SAF. No heat flow anomaly was detected and has been interpreted as indicating low average shear stress [*Williams et al.*, 2004]. Borehole breakout and drilling-induced tensile fractures in the pilot hole at depths below 2050 m indicate that the maximum horizontal stress is inclined at a relatively high angle of $\sim 70^\circ$ to the strike of the SAF [*Hickman and Zoback*, 2004]. In this paper we will follow the nomenclature used by *Rice* [1992] and refer to the complement of this angle, ψ , as the angle between the fault normal and the maximum compressive horizontal stress σ_H . The main borehole (immediately adjacent to the pilot hole) was drilled during SAFOD phase 1 (in 2004) and phase 2 (in 2005). This hole was first drilled vertically to a depth of 1490 m, and then directionally drilled to the northeast toward the SAF, deviating from the vertical at an angle of $54^\circ - 60^\circ$. The main hole terminates at a total vertical depth of 3200 m, corresponding to a measured depth of ~ 4 km. *Boness and Zoback* [2006] inferred from observation of stress-induced seismic anisotropy in the main hole that the maximum horizontal stress basically aligns with that for the deeper portion of the pilot hole as inferred by *Hickman and Zoback* [2004].

[6] The directionally drilled segment of the SAFOD hole penetrated over 1 km of arkosic sandstones and conglomerates, as well as numerous faults before terminating in sedimentary rocks of the Great Valley sequence. Frictional properties of drill cuttings and cores retrieved during phases 1 and 2 were systematically investigated by *Tembe et al.* [2006], who observed that the frictional strength varies appreciably among the primary lithologic units and

shear zones. Whereas the friction coefficients of quartzofeldspathic core and cuttings are in basic agreement with Byerlee's rule, friction coefficients of shale, claystone and siltstone units are lower (in the range of 0.40 to 0.55). Some of the weakest samples were retrieved from two shear zones at measured depths of 2560 m and 3067 m. The active trace of the SAF was penetrated at a measured depth of 3322 m, where minor amounts of talc (which has a very low friction coefficient 0.1 to 0.15) were discovered in serpentinite cuttings [*Moore and Rymer*, 2007].

[7] For the sake of simplicity, *Rice's* [1992] conceptual model (Figure 1a) assumed that the friction coefficient of the fault gouge was comparable to that of the country rock (thus obeying Byerlee's rule). In light of the recent findings that the SAFOD cores contain weak hydrous platy minerals, one objective of the present study is to extend the *Rice*-style model to apply to a fault zone with relatively low frictional strength. Explicit expressions for the stress state and pore pressure distribution will be developed. However, to connect the theoretical predictions to field observations, it is necessary to prescribe the friction coefficient of the SAF gouge as a function of depth. Friction measurements of cuttings and core reported by *Tembe et al.* [2006] were conducted at room temperature, but frictional strengths of minerals such as illite, smectite and serpentine found in SAFOD cores [*Solum et al.*, 2006] tend to increase with increasing temperature and can crystallize into more stable phases [e.g., *Rutter and Maddock*, 1992; *Moore et al.*, 1996, 1997; *Lockner and Beeler*, 2002; *Moore and Lockner*, 2007, 2008]. Hence a second objective of this study is to measure the frictional properties of fault gouge obtained from SAFOD phase 1 cores under hydrothermal conditions comparable to those at seismogenic depths. These results, along with published data on serpentinite and talc, are applied to the modified *Rice* model to determine the combinations of material strengths and fault zone pore pressures that are required to conform to the heat flow and stress orientation constraints proposed for the SAF.

2. Stress State and Pore Pressure Distribution in the Fault Zone

2.1. Stress State in the Country Rock

[8] In this section we develop generalized relationships between fault zone parameters for strike-slip geometry relevant to the San Andreas Fault. Following *Rice* [1992], we will represent properties related to the host rock and fault zone separately. The parameters σ_{ij} , p_o , and μ are stress, pore pressure, and friction coefficient for the host rock, respectively. Key stress components become vertical stress σ_V and maximum and minimum horizontal stress σ_H and σ_h . The parameter σ_H makes an angle ψ with the normal to the fault (Figure 2). The corresponding parameters for the fault zone are denoted by the superscript f , and relevant fault zone parameters become σ'_V , σ'_H , σ'_h , p_f , and μ_f . Horizontal shear and normal stress components in the plane of the fault are denoted by τ and σ_n . With so many relevant parameters, it is no surprise that the problem is essentially underconstrained, and our analysis involves an examination of the combinations of parameters that are consistent with the current observations for the San Andreas system, particularly in the SAFOD region. Ultimately, fault

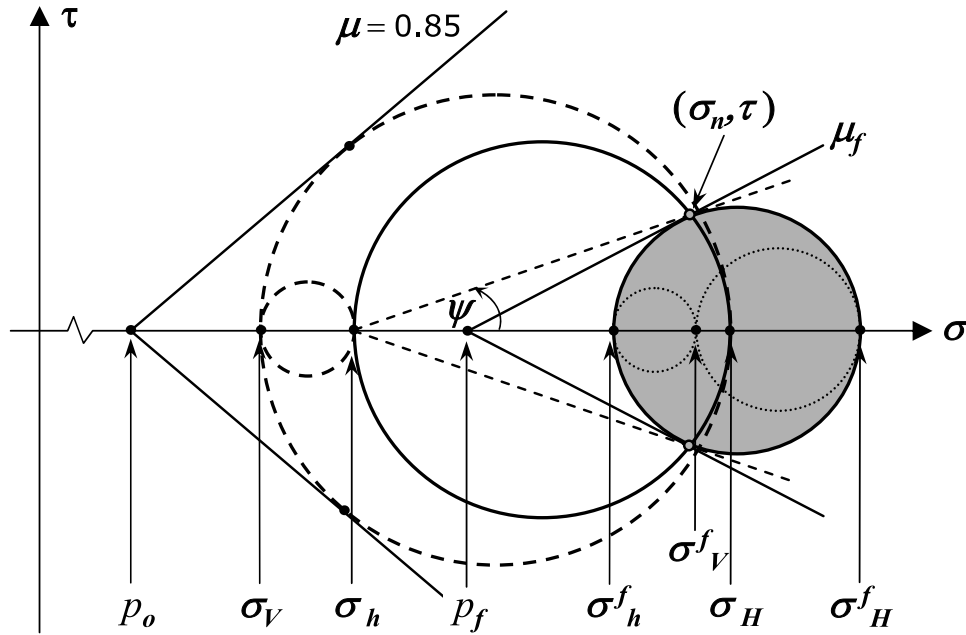


Figure 2. Mohr circle diagram modified after Rice [1992] shows a critically stressed crust in a thrust faulting regime (represented by the large dashed circle) and a critically stressed fault under strike-slip failure (gray circle). The intermediate stress σ_h in the country rock is unconstrained but can be related to the maximum horizontal stress σ_H and vertical stress σ_V by the parameter r in equation (2). The horizontal principal stresses in the country rock are represented by the solid line Mohr circle. The dashed line at angle ψ intersects this Mohr circle at a point corresponding to the shear and normal stresses, which should be continuous across the interface between fault and country rock. The tangent that touches the gray circle at this point is inclined at a slope corresponding to the friction coefficient μ_f of the fault zone. Where this tangent intersects the horizontal axis determines the fault zone pore pressure. In the original Rice [1992] model $\mu = \mu_f$, while in our modified version the fault zone coefficient is allowed to vary, with the friction coefficient of the country rock fixed at 0.85. The diagram is drawn to scale for $r = 0.8$, $\mu = 0.85$, and $\psi = 20^\circ$.

mechanics are reduced to the interplay between stress orientation ψ , minimum horizontal stress σ_h , fault zone overpressure p_f/p_o , and depth-dependent friction μ and μ_f .

[9] In this paper we repeatedly refer to the Rice [1992] model. By this we mean the stress analysis, indicated in Figure 2, in which stresses inside and outside of the fault zone are linked by tractions on the fault surfaces. The final portion of Rice's [1992] paper was devoted to a particular model for sustaining elevated pore fluid pressure within the fault core. This pore fluid model is not what we are considering in our analysis. We are not concerned with particular mechanisms that might produce elevated pore pressure. There are many to choose from, such as, a deep-rooted fault [Rice, 1992], threshold pressure gradient [Byerlee, 1990], transient pore pressure [Sibson, 1990; Byerlee, 1992; Sleep and Blanpied, 1992] or dynamic thermal pressurization [Andrews, 2002], to name a few. Our analysis simply indicates the range of pore pressure that is consistent with values of other model parameters.

[10] Following Rice [1992], we assume that the SAF is in a transpressional stress state so that the minimum and maximum principal stresses are given by the vertical stress σ_V and maximum horizontal stress σ_H , respectively. If the rock mass is permeated by randomly distributed fractures and the pore pressure p_o as a function of depth is given by the hydrostatic gradient, then limiting values of σ_V and σ_H

(represented by the large Mohr circle on the left in Figure 2) are related by [Brace and Kohlstedt, 1980]

$$\sigma_H = \sigma_V \left[\frac{\sqrt{1 + \mu^2} + \mu}{\sqrt{1 + \mu^2} - \mu} \right] - 2p_o \left[\frac{\mu}{\sqrt{1 + \mu^2} - \mu} \right] \quad (1)$$

where μ denotes friction coefficient of the country rock (assumed for now to obey Byerlee's [1978] rule). Fluid and rock density values of $\rho_w = 1000 \text{ kg/m}^3$ and $\rho_r = 2500 \text{ kg/m}^3$ will be used to calculate the pore pressure $p_o = \rho_w g z$ and vertical overburden $\sigma_V = \rho_r g z$. Since the country rock is assumed to be in a thrust faulting regime, the minimum horizontal stress σ_h must be intermediate between σ_V and σ_H . Accordingly, σ_h can be related to σ_V and σ_H by the ratio

$$r \equiv \frac{(\sigma_H - \sigma_h)}{(\sigma_H - \sigma_V)} \quad (2)$$

with allowable values ranging from $r = 0$ ($\sigma_h = \sigma_H$) to $r = 1$ ($\sigma_h = \sigma_V$). Hardebeck and Michael [2004] present a similar but abbreviated fault zone stress analysis in which σ_h is treated implicitly. Because of the importance that σ_h can have in defining fault zone characteristics, we preserve it as an explicit parameter. While σ_H can be calculated from σ_V and μ through the Coulomb failure criterion (Figure 2), constraints on σ_h turn out to be more problematic. Without further mechanical constraints associated with the transpres-

sional geometry that can be imposed, σ_h is limited only by parameter r with values $0 \leq r \leq 1$. However, *Hickman and Zoback* [2004] inferred from observations of breakouts and tensile fractures in the SAFOD pilot hole that σ_h is comparable to the vertical overburden, corresponding to a ratio of $r \approx 0.8$ to 1.

2.2. Stress State and Pore Pressure Inside the Fault Zone

[11] A conceptual breakthrough in *Rice's* [1992] and *Byerlee's* [1990] analyses is the clear differentiation between stress states in the country rock and within the gouge zone. Rice emphasized that the two stress tensors can be very different, and indeed it is quite possible to have the fault zone undergoing strike slip deformation (represented by the gray Mohr circle in Figure 2) while embedded in an overall thrust environment. Analysis of the Mohr circle construction in Figure 2 shows that the horizontal normal and shear stresses (σ_n, τ) on the fault plane are completely determined from the stress state in the host rock. We assume that at a given depth σ_V, p_o and μ are known and therefore σ_H can be calculated. Then, for given r and ψ , the point (σ_n, τ) is fixed by the standard construction of the dashed line extending at angle ψ from the point ($\sigma_h, 0$).

[12] The stress states in the fault and country rock are coupled by mechanical equilibrium at the interface between the gouge zone and the country rock, such that σ_n and τ are continuous across the interface. Thus, the stress state of the fault zone is determined uniquely by the fault-parallel stresses (σ_n, τ) and the fault friction coefficient μ_f . That is, the Mohr circle representing the horizontal stress state of the fault must pass through the point (σ_n, τ) where it is also tangent to a Coulomb yield surface with slope μ_f . Strike-slip failure of the fault zone further requires the horizontal stress state in the gouge to have the minimum and maximum principal stresses of σ_h^f , and σ_H^f , respectively. The vertical stress in the fault zone σ_V^f is the intermediate stress and can range in value between σ_h^f , and σ_H^f , although there is little to constrain this better.

[13] As mentioned above, *Rice* [1992] assumed $\mu_f = \mu$ for the sake of simplicity. Since we will consider weak fault gouge materials, we relax this constraint and allow $\mu_f \leq \mu$. The yield surface tangent to the fault zone stress circle (gray circle in Figure 2) intersects the horizontal axis at p_f , the pore pressure within the fault gouge. It can be observed that not only are the stress states within and outside the fault zone very different, the pore pressure p_f inside the fault zone is also significantly higher than the hydrostatic value p_o in the country rock. Indeed, it is possible that the local pressure p_f exceeds the lithostatic pressure σ_V . However, it should also be noted that even though the local pore pressure can be very large, hydraulic fracturing does not occur since its magnitude is still less than the minimum principal stress σ_h^f inside the fault gouge zone, consistent with the result obtained by *Byerlee* [1990] and *Rice* [1992]. As noted above, stresses acting in the plane of the fault (σ_n, τ) are completely determined by properties of the country rock. Since yielding of the fault requires that the fault failure envelope pass through the point (σ_n, τ), the fault zone failure envelope is required to pivot about this point with slope μ_f . As expected, the result is that a small μ_f (weaker fault gouge) is linked to lower fault zone pore pressure.

[14] Analytic expressions can be derived for the pore pressure and stresses inside the fault zone. The mathematical details are described in Appendix A, and here we only present the pertinent results. The resolved shear and normal stresses are given by

$$\tau = \frac{r\mu \sin 2\psi}{\sqrt{1 + \mu^2} - \mu} (\sigma_V - p_o) \quad (3)$$

$$\sigma_n = p_o + \left[\frac{\sqrt{1 + \mu^2} + \mu - r\mu \sin^2 \psi}{\sqrt{1 + \mu^2} - \mu} \right] (\sigma_V - p_o) \quad (4)$$

[15] Since in the host rock the overburden σ_V and hydrostatic pore pressure p_o both increase linearly with depth z , the resolved shear and normal stresses would also increase linearly with depth for fixed friction coefficient μ and angle ψ . It should be noted in (3) that the horizontal shear stress resolved parallel to the fault is directly proportional to r , and therefore arbitrarily low shear stress can be attained for r very small ($\sigma_h \approx \sigma_H$), independent of stress orientation or friction coefficient. Expressions for the maximum and minimum horizontal stresses are given in Appendix A.

[16] We next focus on the pore pressure inside the fault zone, which is given by

$$p_f = p_o + \left[\frac{\sqrt{1 + \mu^2} + \mu - r\mu (\sin^2 \psi + \sin 2\psi/\mu_f)}{\sqrt{1 + \mu^2} - \mu} \right] (\sigma_V - p_o) \quad (5)$$

The local pore pressure excess (given by the second term above) derives from the trade-off between the orientation of remote stresses ψ and friction coefficient μ_f . This pore pressure excess within the fault zone will not, in general, increase linearly with depth unless both μ and μ_f are independent of temperature and effective normal stress. We plot in Figure 3 the Hubbert-Rubey coefficient $\lambda = p_f/\sigma_V$ as a function of the angle ψ for friction coefficient μ_f ranging from 0.1 to 0.6. It can be seen that while the pore pressure excess increases with increasing frictional strength, it decreases almost linearly with increasing angle. As elaborated in Appendix A, if the angle ψ is small ($<20^\circ$ or so), the term containing $\sin^2 \psi$ in (5) can be neglected and $\sin 2\psi$ can be approximated by 2ψ . Accordingly, the local pore pressure can be approximated by

$$p_f \approx p_o + \left[\frac{\sqrt{1 + \mu^2} + \mu - 2\mu (r\psi/\mu_f)}{\sqrt{1 + \mu^2} - \mu} \right] (\sigma_V - p_o) \quad (6a)$$

and therefore the Hubbert-Rubey coefficient is simply

$$\lambda = \frac{p_f}{\sigma_V} \approx \frac{\rho_w}{\rho_r} + \left(1 - \frac{\rho_w}{\rho_r} \right) \left[\frac{\sqrt{1 + \mu^2} + \mu - 2\mu (r\psi/\mu_f)}{\sqrt{1 + \mu^2} - \mu} \right]. \quad (6b)$$

The pore pressure excess decreases linearly with increasing $r\psi/\mu_f$, a parameter that characterizes the interplay of the

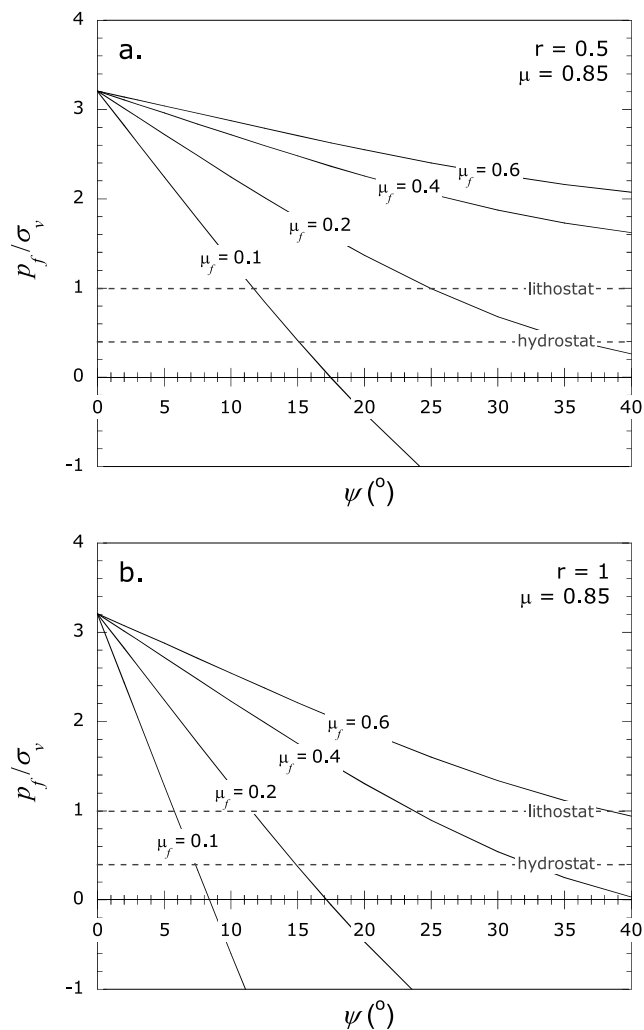


Figure 3. Hubbert-Rubey pore pressure coefficient $\lambda = p_f/\sigma_v$ for the fault zone as a function of the fault angle for a range of friction coefficients μ_f , with the country rock friction coefficient μ fixed at 0.85. The pore pressure coefficient was evaluated using equation (5) for two stress ratios: (a) $r = 0.5$ and (b) $r = 1$. The pore pressure excess is predicted to increase with increasing friction coefficient and decreasing fault angle. For reference the Hubbert-Rubey coefficients corresponding to hydrostatic and lithostatic pore pressures are represented by the two dashed lines. Coefficient values below zero are not physically permissible.

fault stress state (in the numerator) and frictional strength (in the denominator).

[17] For near fault normal compression, we can use (6b) to evaluate the parameter $r\psi/\mu_f$ for the limiting case of $\lambda = \rho_w/\rho_r$ (corresponding to hydrostatic pore pressure within the fault):

$$\frac{r\psi}{\mu_f} \approx \frac{\sqrt{1 + \mu^2} + \mu}{2\mu} \quad (7)$$

which ranges from 1.27 to 1.47 for $\mu = 0.85$ to 0.6. If we assume $\psi = 20^\circ = 0.35$ radians (as inferred by Hickman and

Zoback [2004] and Boness and Zoback [2006]), then the maximum gouge friction value that satisfies this condition is $\mu_f = 0.28$ (for $\mu = 0.85$ and $r = 1$). More likely parameter values might be $\psi = 20^\circ$, $\mu = 0.55$ and $r = 0.9$, implying $\mu_f = 0.20$. In other words, pore pressure excess would be negligible only if gouge friction coefficient μ_f is less than about 0.2. Since the room temperature laboratory data for the SAFOD cuttings and cores [Tembe et al., 2006; Morrow et al., 2007] indicate higher friction coefficients, it seems likely that pore pressure excess (Figure 1a) must be invoked in conjunction with intrinsic gouge weakness (Figure 1b) to satisfy near fault normal compression at SAFOD. Alternatively, dynamic weakening mechanisms might be invoked to achieve this low sliding strength.

[18] To characterize better the frictional strength of the SAF gouge as a function of depth, we conducted a suite of hydrothermal experiments to investigate the frictional properties of a SAFOD core. The new data along with other published data will be incorporated in this model to infer the stress state and pore pressure distribution that are compatible with the stress orientation and heat flow measurements at SAFOD.

3. Laboratory Frictional Strength and Near-Fault Normal Compression

[19] In section 2, we quantified the trade-off between low shear strength and high fluid pressure in satisfying heat flow and stress orientation constraints for the SAF. We now consider three candidate mineralogies associated with the SAF at Parkfield and the degree to which their pressure- and temperature-dependent rheologies are consistent with these constraints. The three materials are serpentinite, pure talc and a natural gouge retrieved from depth during SAFOD drilling.

[20] In their investigation of the room temperature frictional strength of cuttings and spot core samples retrieved during SAFOD phases 1 and 2, Tembe et al. [2006] found that the weakest material encountered was from a clay-rich layer (see Appendix B) ~ 30 cm thick in the spot core at a measured depth (MD) of 3067 m. The black gouge (cut from a zone 7 to 9 cm from the top of the core) had a friction coefficient of 0.40–0.45 at room temperature and was more than 50% illite and mixed layer clays. The shear zone is thought to be a minor inactive strand ~ 130 m southwest of the active SAF [Hickman et al., 2005]. Characteristics of this clay-rich gouge are described in more detail in Appendix B. While core samples of the active trace of the SAF were retrieved during phase 3 drilling, these samples have not yet been released for laboratory mechanical testing. In the meantime, we felt that the weak “black gouge” material from 3067 m MD, while not the ideal material, was taken from depth close to the active fault trace and might serve as an interim proxy for SAF gouge. We therefore proceeded to measure frictional strength of this black gouge under hydrothermal conditions representative of burial depth to 15.3 km. Details of these measurements are provided in Appendix B. In phase 2 drilling, the active trace of the SAF was penetrated at 3322 m MD, where serpentinite cuttings were retrieved and talc discovered [Moore and Rymer, 2007]. Since neither of these minerals was present in the 3067 m black gouge, we decided to expand our analysis of fault zone

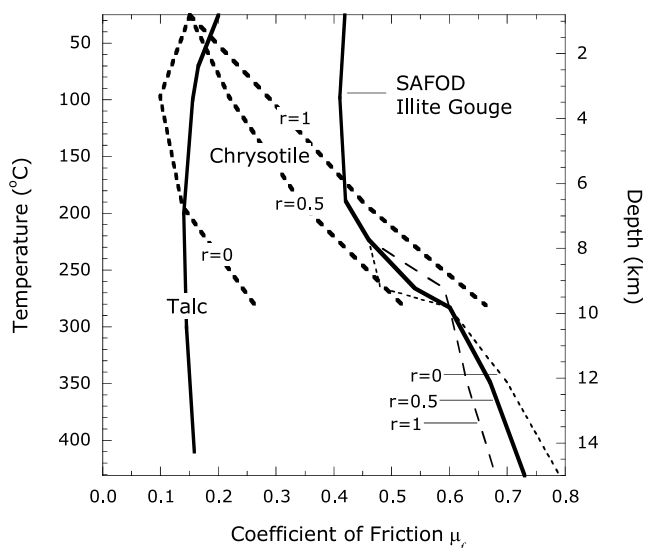


Figure 4. The coefficient of friction μ_f as a function of temperature and depth for three fault zone materials considered in our analysis. We plot for each material the temperature dependence of friction for three stress ratios ($r = 0, 0.5,$ and 1) inferred from laboratory data using the approach summarized in Appendix B. The data show that friction coefficient is sensitive to both temperature and effective normal stress. In our model the pore pressure (and the effective normal stress) is sensitively dependent on the stress ratio r , and accordingly, the friction coefficient at a given temperature is also sensitive to r . Of the three gouge types, talc has the least temperature and pressure dependence of friction and is the weakest overall. The geothermal regime can be approximated by a linear gradient of $\sim 28^\circ\text{C}/\text{km}$ (Appendix C), which is used to relate temperature to depth.

stresses to include laboratory data on serpentinite and talc [Reinen *et al.*, 1991, 1994; Moore *et al.*, 1996, 1997, 2004; Moore and Lockner, 2007; Escartin *et al.*, 2008; Moore and Lockner, 2008].

3.1. Friction Coefficient as a Function of Depth Constrained by Laboratory Data

[21] Seismological and geological indicators constrain the maximum horizontal stress near SAFOD to be at a high angle to the strike of the SAF [e.g., Mount and Suppe, 1987; Zoback *et al.*, 1987] as suggested in Figure 2. While governing equations (3), (4), and (5) are quite general, we will assume in most of our calculations a value of $\psi = 20^\circ$ to be consistent with data derived from borehole breakouts and drilling-induced tensile fractures in the SAFOD pilot hole [Hickman and Zoback, 2004] as well as stress-induced seismic anisotropy in the main hole [Boness and Zoback, 2006].

[22] Equations (3) and (4) were used to evaluate the shear stress and normal stress inside the fault zone. For most of our calculations we fixed $\psi = 20^\circ$, $\mu = 0.85$, $\rho_w = 1000 \text{ kg/m}^3$ and $\rho_r = 2500 \text{ kg/m}^3$. The minimum horizontal stress in the country rock is represented by the parameter r . To analyze its influence, we will show calculations for $r = 0$ ($\sigma_h = \sigma_H$), 0.5 , and 1 ($\sigma_h = \sigma_V$). Pore pressure inside the fault zone is computed using (5) and requires specification of the depth

dependence (and therefore normal stress and temperature dependence) of the gouge friction coefficient μ_f . Friction data for the three gouge types, as used in the calculations, are shown in Figure 4. For details of how the strength versus depth curves were determined, see Appendix B. While the SAFOD black gouge was more than 50 percent clay, it also contained a significant portion of strong minerals. As a result, room temperature strength was the strongest of the three gouge types considered. The black gouge showed little temperature or pressure sensitivity until about 200°C ($\sim 7 \text{ km}$). Strength then increased steadily with temperature to an equivalent depth of 15 km. The highest temperatures tested (up to 431°C) were out of the stability field of the illite and mixed layer constituents. A thorough analysis would require detailed measurements of phase conversions and reaction rates and is outside the scope of the present study. Muscovite and other hydrous reaction products are unlikely to be weaker than the low-temperature phases. Therefore, in the context of the present analysis, the black gouge, as a proxy for SAF fault zone material, is not weak under shallow crustal conditions and is likely to become even stronger under conditions of increasing pressure and temperature.

[23] The strength data summarized in Figure 4 were determined by first defining temperature as a function of depth with a geothermal gradient that is considered to be appropriate for the SAF near Parkfield. As detailed in Appendix C, the geotherm (C1) we used was originally proposed by Lachenbruch and Sass [1977], with parameters constrained by SAF heat flow data of Sass *et al.* [1997], Williams [1996], and Williams *et al.* [2004]. The temperature variation as a function of depth is approximately linear with a gradient of $\sim 28^\circ\text{C}/\text{km}$. The pore pressure was evaluated using (5) at depths corresponding to the temperatures at which the friction data were acquired (Table 1). However, the gouge friction coefficient μ_f at a given temperature is not constant. Rather, for the black gouge, and to a much larger degree for chrysotile [Moore *et al.*, 1996], coefficient of friction is sensitive to effective normal stress. Since effective normal stress at a given depth will depend on σ_h , and therefore on r , different depth-friction profiles are required for different r values.

[24] Figure 5a shows the shear and normal stresses according to (3) and (4). As noted in section 2.2, these

Table 1. Summary of Experimental Conditions^a

Run	Temperature (°C)	Depth (km)	$\sigma_n - p_f$ (MPa)	τ (MPa)	μ_f at 3.2 mm Axial Displacement	$a - b$
1	96	3.0	38	12	0.41	0.0070
12	100	3.15	75	31	0.40	0.0107
2	189	6.3	76	32	0.42	0.0063
4	223	7.5	95	44	0.46	0.0035
8	266	9.0	76	38	0.50	-0.0043
7	266	9.0	113	62	0.54	-0.0056
11	266	9.0	226	129	0.57	-0.0013
3	283	9.6	113	68	0.60	-0.0043
9	349	12.0	100	68	0.68	-0.0006
5	349	12.0	150	102	0.68	0.0068
10	349	12.0	300	197	0.65	0.0122
6	431	15.0	188	137	0.73	0.0115

^aOne standard deviation for uncertainty in $a - b$ is ± 0.0006 .

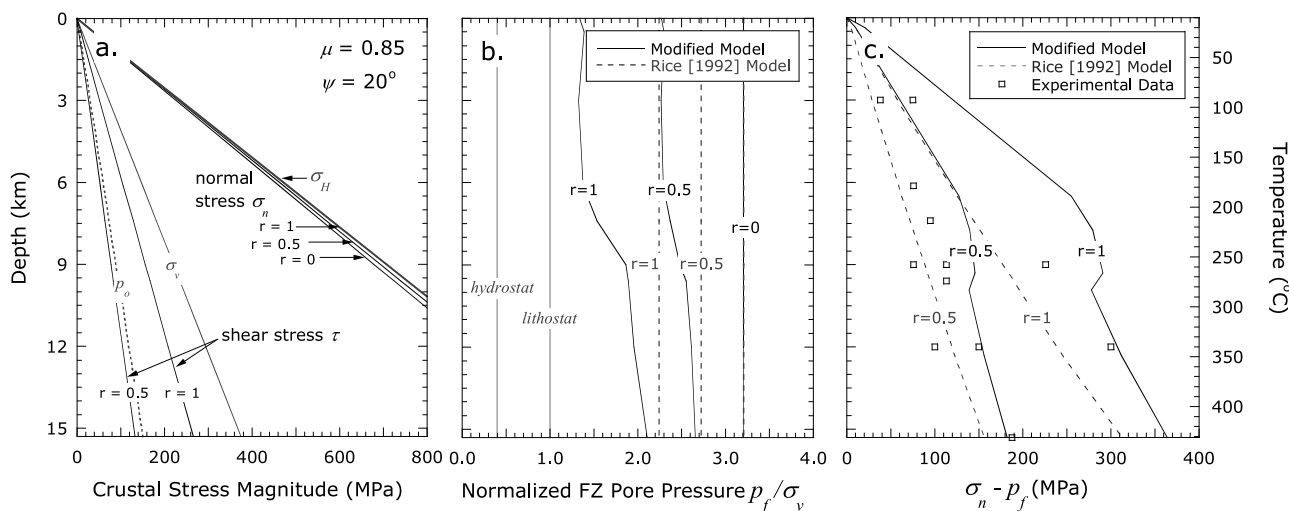


Figure 5. (a) Shear and normal stresses resolved on the fault as functions of depth for $r = 0, 0.5$, and 1 . In our model these stresses are independent of fault zone parameters. They increase linearly with depth according to equations (3) and (4). (b) Normalized fluid pressure (in terms of the Hubbert-Rubey coefficient) as a function of depth for $r = 0, 0.5$, and 1 in an illite-rich fault zone obtained by the modified (solid lines) and original Rice [1992] models (dashed lines). The hydrostat and lithostat are included for reference. (c) Effective normal stress in the fault zone as a function of depth for $r = 0.5$ and 1 in an illite-rich fault zone obtained by the modified (solid lines) and original Rice [1992] models (dashed lines). The effective normal stress and temperature (equivalent to depth) at which we conducted our friction experiments are indicated by the symbols.

stresses are determined by conditions in the host rock, regardless of gouge properties and increase linearly with depth. For comparison we also include the two lines corresponding to lithostatic and hydrostatic stress gradients. Since the shear stress is directly proportional to r , its maximum magnitude is attained if $\sigma_h = \sigma_v$ ($r = 1$). In contrast, the normal stress is nearly independent of the stress ratio and as noted in Appendix A, normal stress can simply be approximately by the maximum horizontal stress σ_H as given by equation (A9).

3.2. Model Results for Pore Pressure Excess in an Illite-Rich Fault Zone

[25] Figure 5b shows the pore pressure (normalized by the overburden stress) for the illite-rich black gouge from SAFOD 3067 m MD, calculated in conjunction with the friction coefficient values in Figure B2b (Appendix B). Several features of the pore pressure distribution should be noted. First, the pore pressure excess is calculated to be less than the scenario originally considered by Rice [1992] for $\mu = \mu_f$. Since frictional strength of the gouge is weaker than the country rock, a lower pore pressure excess is involved for failure of a fault zone under near fault normal compression. Nevertheless, the pore pressure required is still very high, well in excess of the lithostatic pressure. Second, because the friction coefficient of the illite-rich gouge increases appreciably with temperature, the calculated pore pressure also increases with depth. Third, the pore pressure excess is sensitive to r , and the minimum pressure is required for $\sigma_h = \sigma_v$ ($r = 1$).

[26] Figure 5c shows the modeled effective normal stress as a function of depth (and temperature). For comparison we also show the effective normal stress and temperature at which our experiments were conducted.

From equation (A10) the effective stress is approximately proportional to r and inversely proportional to μ_f . Accordingly effective normal stress decreases with depth in the 8 to 10 km range because the gouge friction coefficient increases rapidly with temperature.

3.3. Model Results for Fluid Pressures in Chrysotile- and Talc-Dominated Fault Zones

[27] Characterization of the serpentinite discovered in SAFOD drill cuttings by Moore and Rymer [2007] showed the presence of the low-temperature serpentinite phases, chrysotile and lizardite. Talc was found to coat vein walls, fill cracks, and form along foliation in sheared serpentinite. Room temperature friction experiments on sheared serpentinite grains plucked from bulk cuttings [Morrow et al., 2007] gave friction coefficients of 0.40–0.45 at 40 MPa effective normal stress. Laboratory studies on the strength [Moore et al., 1996, 1997] and velocity dependence [Moore et al., 1997, 2004] of chrysotile show sensitivity to temperature, normal stress and displacement rate. Given the possible significance of these minerals in the mechanics of the San Andreas Fault, we will model the pore pressure distribution for chrysotile and talc. In the interest of brevity we are not including lizardite in our analysis since its coefficient of friction (0.42–0.52 over 25–200 $^\circ\text{C}$) is similar to the black gouge and would require excess fault zone pore pressure of similar magnitude.

[28] Frictional data obtained in the saw cut geometry for chrysotile were reported by Moore et al. [1996, 1997, 2004] for effective normal stresses between 40 and 200 MPa and temperatures of 25–280 $^\circ\text{C}$ (0.5–9.5 km). Chrysotile has a distinct hydrophilic quality due to a relatively large specific surface area and a unique tubular structure that exposes an (OH) $^-$ layer on the surface [Moore et al., 2004]. Thus,

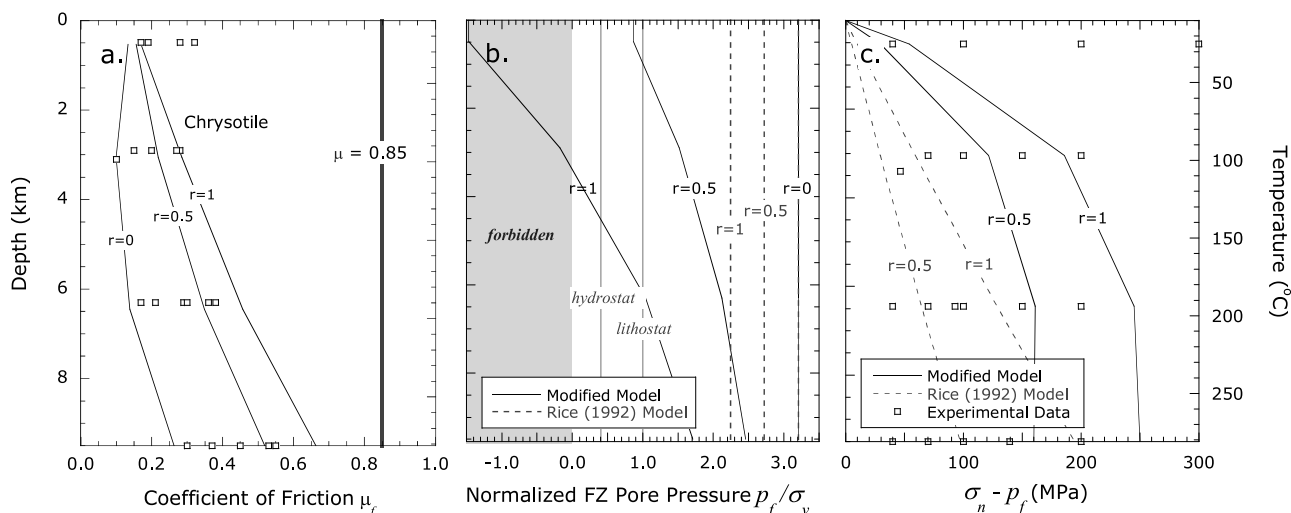


Figure 6. (a) Friction coefficient of chrysotile as a function of depth and stress ratio inferred from laboratory data. (b) Normalized fluid pressure (in terms of the Hubbert-Rubey coefficient) as a function of depth for $r = 0, 0.5$ and 1 in a chrysotile fault zone obtained by the modified (solid lines) and original *Rice* [1992] models (dashed lines). The hydrostat and lithostat are included for reference. (c) Effective normal stress in the fault zone as a function of depth for $r = 0.5$ and 1 in a chrysotile fault zone obtained by the modified (solid lines) and original *Rice* [1992] models (dashed lines). The effective normal stress and temperature (equivalent to depth) for laboratory data are indicated by the symbols.

water-saturated chrysotile at low pressure and temperature has a friction coefficient of 0.15 that gradually reaches 0.55 as adsorbed water is driven off with increasing pressure and temperature.

[29] Figure 6a compiles the chrysotile friction data of *Moore et al.* [1996, 1997, 2004] obtained from room temperature to 280°C for several effective normal stresses. We used the linear interpolation approach described in Appendix B to simultaneously solve for the effective normal stress and friction coefficient at each temperature. The calculated friction coefficients as a function of depth for $r = 0, 0.5$ and 1 are shown by the solid lines in Figure 6a. The frictional strength of chrysotile is appreciably lower than the SAFOD black gouge (Figure 4), and consequently lower pore pressures are required to achieve failure under near fault normal compression. Indeed, for very small values of μ_f and ψ a formal application of the model would require negative pore pressure (Figure 3), which is not physically realistic. We also show in Figure 6c the effective normal stress as a function of depth, and for comparison the effective normal stress and temperature at which the experimental data were acquired.

[30] Talc is typically found in mineral assemblages containing serpentine and brucite and is considered to replace serpentine by reaction with silica. It is thought to form in the mantle wedge above a subducting slab as silica-rich fluids migrate upward causing serpentinization of the overlying rock. Unlike the hydrous clays (i.e., smectite) and the serpentine minerals, talc remains weak well into the brittle crust (to depths of 15 to 20 km). Frictional strength data for water-saturated talc obtained in the same manner and apparatus used for the SAFOD ST1 3067 m MD gouge, were reported by *Moore and Lockner* [2007, 2008]. Dry talc friction coefficients were in the 0.2 to 0.35 range, in comparison to wet runs that had strengths around 0.15 to

0.2. Velocity strengthening was observed at all the conditions tested.

[31] Figure 7a compiles the talc friction data of *Moore and Lockner* [2007, 2008] obtained at room temperature, 100°C, 200°C, 300°C, and 400°C for several effective normal stresses. Since the friction coefficient is very low, it can be seen from (A10) that high pore pressures are not necessary for fault zone yielding and effective normal stress increases to hundreds of MPa. Since the effective normal stresses in the laboratory tests were lower, the interpolation scheme (Figure B2a) cannot be applied here. In our calculations we simply used the mean value of the friction coefficients measured at a given temperature, thus neglecting the very small dependence on effective normal stress. Figure 7b presents the pore pressure distribution and Figure 7c the effective normal stress as a function of depth. Because of the extremely low strength of talc, the pore pressures required are quite low but the effective normal stress can rise to ~ 1 GPa at 13 km.

4. Discussion

4.1. Fault Normal Compression, Frictional Strength, and Pore Pressure Excess

[32] *Rice* [1992] proposed a model whereby frictional failure in a nominally strong fault may occur under near fault normal compression in the presence of pore pressure excess. Motivated by observations from SAFOD that the gouge may contain clay minerals such as illite and smectite (which lower the friction coefficient to 0.4 or less) and trace amount of talc (with friction coefficient down to 0.1), we extend *Rice's* model to consider a scenario with a lower friction coefficient in the main fault zone than in subsidiary faults in the host rock. This extension is fully consistent with the framework developed by *Rice* [1992] and more recently discussed by *Hardebeck and Michael* [2004]. We

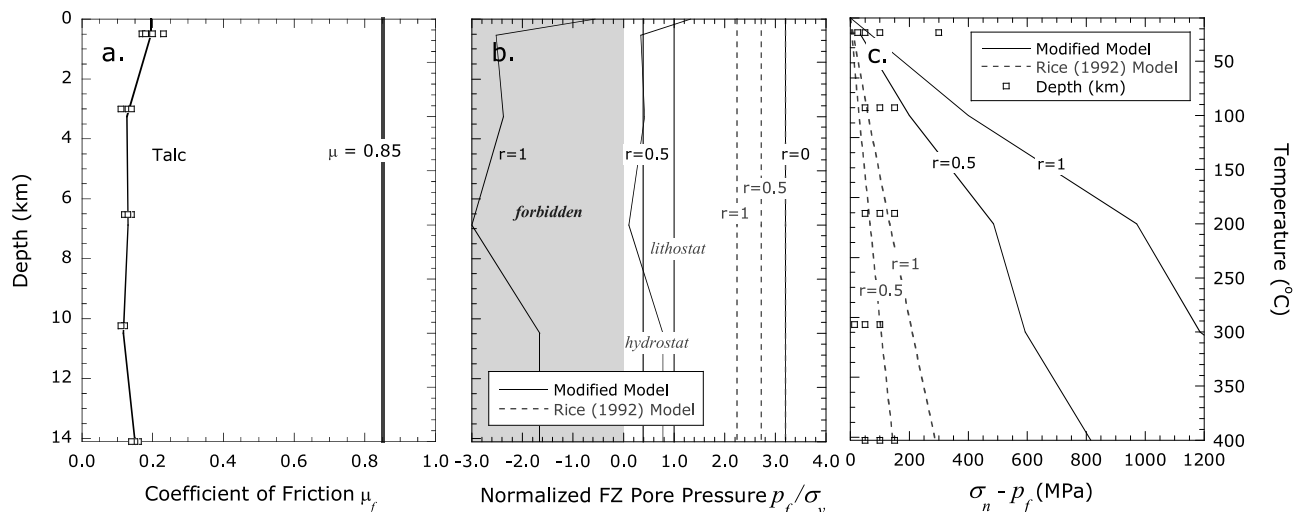


Figure 7. (a) Friction coefficient of talc as a function of depth inferred from laboratory data. Since the interpolation scheme could not be applied to talc, an average value independent of r was used in the model. (b) Normalized fluid pressure (in terms of the Hubbert-Rubey coefficient) as a function of depth for $r = 0, 0.5$, and 1 in a talc fault zone obtained by the modified (solid lines) and original *Rice* [1992] models (dashed lines). The hydrostat and lithostat are included for reference. (c) Effective normal stress in the fault zone as a function of depth for $r = 0.5$ and 1 in a talc fault zone obtained by the modified (solid lines) and original *Rice* [1992] models (dashed lines). The effective normal stress and temperature (equivalent to depth) for laboratory data are indicated by the symbols.

have also conducted high-temperature experiments on one of the weakest gouge samples retrieved from SAFOD phase 1 and 2 drilling to determine frictional properties pertinent to seismogenic depths. To our knowledge, this is the first experimental study of the frictional properties of a natural clay-rich gouge under hydrothermal conditions. Both SAFOD phase 2 and 3 drilling indicates that serpentine and possibly talc are closely associated with the active traces of the San Andreas Fault at 3 km depth. We therefore included pure chrysotile and pure talc data in our analysis since these are both low-strength minerals and may be important in controlling stress and deformation state of the SAF system, especially in the creeping sections.

[33] Our modeling using the hydrothermal friction data of the SAFOD black gouge from 3067 m MD calculates a pore pressure that is less than that in the strong gouge scenario originally considered by *Rice* [1992]. Nevertheless, the pore pressure required is still high, well in excess of the lithostatic pressure (Figure 5). Because the friction coefficient of the illite-rich gouge increases appreciably with temperature, the calculated pore pressure needed to promote yielding also increases with depth. This result is in apparent discrepancy with borehole observations at SAFOD, which have yet to detect such pressure excesses (S. Hickman, personal communication, 2007). The possibility remains that pore pressure in the undisturbed fault gouge is superlithostatic but, due to low permeability, is not detectable at the borehole. It is also possible that deeper in the fault zone, where temperature and pressure are higher, fault zone sealing mechanisms take over and lead to overpressure that is not present at 3 km depth [Sibson, 1990; Byerlee, 1992; Morrow *et al.*, 2001]. Still, the fact remains that no significant overpressure was detected during the SAFOD drilling operation.

[34] If further measurements at SAFOD confirm the absence of pore pressure excess, an important question that must be addressed is what frictional strength and stress state can be compatible with near fault normal compression and hydrostatic pore pressure. For the fault architecture and stress states considered here, the pore pressure distribution (5) depends on the stress state and orientation, as well as gouge friction coefficient. We illustrate in Figure 8 the trade-off among these factors. The angle ψ characterizing the stress orientation is plotted as a function of the gouge friction coefficient μ_f for four different values of the Hubbert-Rubey coefficient λ . For near fault normal compression (with $\psi = 20^\circ$ or so) the modeled pore pressure is hydrostatic only if the fault zone has an abundance of relatively weak minerals such as talc and chrysotile. In Figure 8 we fixed $r = 0.8$ and the coefficient of friction of the host rock for $\mu = 0.85$ and $\mu = 0.55$. If the stress state is such that $r \rightarrow 1$ (or $\sigma_h \rightarrow \sigma_v$), near hydrostatic pore pressure is viable even if the gouge friction coefficient is somewhat higher, but then the shear stress τ (which is proportional to r) will become even higher, rendering it more difficult to satisfy the heat flow constraint on the stress magnitude.

[35] While our analysis underscores that the model calculations on both shear stress and pore pressure are very sensitive to the stress state (as parameterized by r), unfortunately very limited SAFOD data are available to constrain this key mechanical attribute. Estimates of stress magnitude are available for the pilot hole, and as noted by *Hickman and Zoback* [2004], significant uncertainty is associated with these stress values primarily inferred from dimensions of borehole breakouts. In the main hole, systematic characterization of the stress orientation was conducted by *Boness and Zoback* [2006] on the basis of stress-induced seismic anisotropy, a technique which is not applicable to some of the more shaly and clay-rich sections in the vicinity of the active fault.

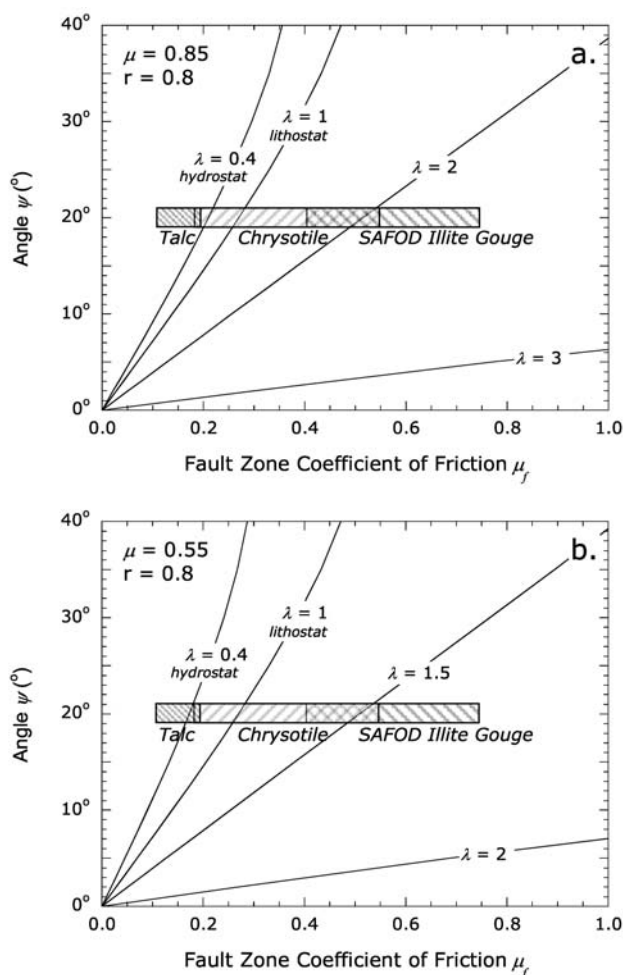


Figure 8. Control of gouge friction coefficient μ_f and fault orientation ψ over pore pressure in a critically stressed fault zone. Two different friction coefficients for the country rock were considered: (a) $\mu = 0.85$ and (b) $\mu = 0.55$. The shaded fields correspond to ranges of friction coefficient for the three gouge materials measured in the laboratory. The stress ratio is fixed at $r = 0.8$ and if we consider $\psi = 20^\circ$ as constrained by the latest SAFOD findings, then the modeled pore pressure is hydrostatic only if the fault zone has an abundance of relatively weak materials such as talc and chrysotile. If the stress state is such that r approaches 1 or if the fault orientation is such that ψ is significantly larger, then hydrostatic pore pressure may be viable for all three gouges, but then the shear stress will become so high that it is very difficult to satisfy the heat flow constraint on stress magnitude.

[36] Notwithstanding the apparent absence of pore pressure excess, detailed analyses of mineral assemblages in SAFOD show pervasive mineralization indicative of significant paleofluid activity [Solum *et al.*, 2006; Schleicher *et al.*, 2006; Solum *et al.*, 2007]. From their noble gas analyses of SAFOD mud gas samples, Wiersberg and Erzinger [2007] suggested that the SAF provides a path for fluid flux from greater depths, but higher amounts of mantle-derived fluids rise up through other, more permeable faults, situated on the North American Plate side of the SAF Zone.

Such a scenario would involve significant spatial complexity in both the fluid flow and stress field, which is not addressed in Rice's [1992] model or in the extended version considered here, since such an analysis focuses on the stress states in the proximity of the interface between fault gouge layer and country rock [Faulkner *et al.*, 2006].

[37] The spatial variation of stresses was captured by a three-dimensional mechanical model of SAFOD developed by Chéry *et al.* [2004]. In particular, the stress orientation and its variation with depth at the pilot hole were simulated in their finite element model of a relatively weak fault embedded in a strong crust and a weak upper mantle with laterally variable heat flow. Their simulations show an abrupt rotation of the stress tensor at the interface between fault gouge and country rock, in basic agreement with Rice's [1992] model predictions. However, since Chéry *et al.* [2004] did not consider pore pressure explicitly, the effects of intrinsic gouge strength and elevated pore pressure are lumped together into an "effective" friction coefficient. A poromechanical model that explicitly accounts for the fault rheology and fluid flow processes will provide additional insights, and a comprehensive characterization of pertinent hydraulic and poromechanical properties of SAFOD cores will also be necessary to help constrain such processes.

4.2. Heat Flow Constraint on Stress State

[38] The lack of a pronounced heat flow anomaly across the SAF is interpreted to require shear stress, when averaged over the upper 14 km of the fault, to be less than about 20 MPa [e.g., Brune *et al.*, 1969; Lachenbruch and Sass, 1980, 1992; Williams *et al.*, 2004]. Observations of near fault normal compression further constrain the average shear stress to about half this level. Our analysis demonstrates that for a Rice [1992]-style model, in which the fault yields at a relatively high friction level ($\mu > 0.6$), near fault normal compression, average shear stresses in the 10–20 MPa level inferred from heat flow measurements [e.g., Lachenbruch and Sass, 1992; Williams *et al.*, 2004] can be attained only if the stress ratio r is relatively small ($\sigma_h \sim \sigma_H$) and pore pressure is very high. Neither of these conditions has been observed at SAFOD. For $r \approx 1$ ($\sigma_h \approx \sigma_V$), a model compatible with fault normal compression that can explain the relative weakness of the SAF may not be sufficiently weak in the absolute sense to satisfy the heat flow constraint. To clarify this issue, we consider the stresses associated with the end-member scenario illustrated in Figure 1b.

[39] In previous examples, we would prescribe σ_V , μ (and therefore σ_H), p_o and ψ in the country rock. This would uniquely determine σ_n and τ for the fault. Then, knowing μ_f for the fault gouge, we would solve for p_f . In the present example, we will instead assume that p_f is hydrostatic and find values of ψ and μ_f that satisfy the model constraints when averaged over the upper 14 km of the fault. The average shear strength of the fault is $\bar{\tau}$, and pore pressures in both the country rock and fault zone are taken to be hydrostatic. Shear stress is assumed to increase linearly to the base of the seismogenic layer of thickness $L = 14$ km (Figure 9a). Mathematical details of this calculation are presented in Appendix D.

[40] We first consider the case for which the country rock is in a thrust faulting regime (Figure 2) as discussed by Rice [1992]. We evaluated the fault angle, effective normal stress

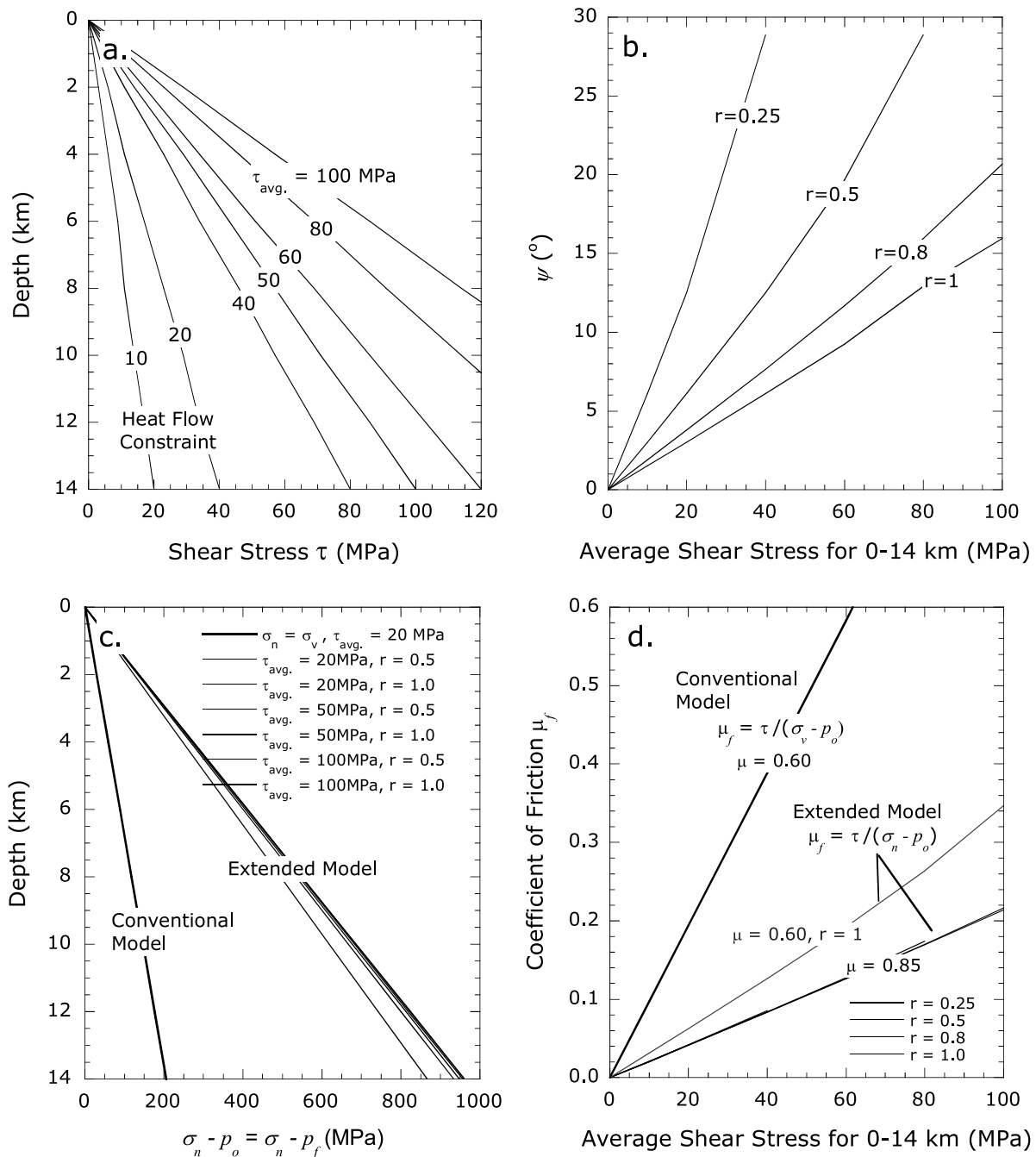


Figure 9. (a) Shear stress as a linear function of depth over a 0–14 km depth interval corresponding to seven average stress values ranging from 10 to 100 MPa. (b) Fault angle as a function of average shear stress as calculated from equation (D2) for four different values of the stress ratio r . To satisfy the heat flow constraint with average shear stress in the 10–20 MPa range and the SAFOD findings of r in the range of 0.8–1, the fault angle must be very small. For a relatively strong fault with average shear stress of 100 MPa and r in the range of 0.8–1, the fault angle would be in the range of 16–21°. (c) Effective normal stress in the fault zone as function of depth. In the conventional model as described by equation (10a), the normal stress is assumed to be equal to the lithostatic and pore pressure is hydrostatic. In our extended model, the stress state in the country rock is in a thrust faulting regime and pore pressure is hydrostatic. The effective normal stress given by equation (D3) is insensitive to the average shear stress and r . (d) With the depth distributions of shear stress and effective normal stress defined in Figures 9a and 9c, the corresponding coefficient of friction for the fault zone can be calculated for the conventional and extended models. The friction coefficients obtained from the extended model are insensitive to r and are significantly lower than the conventional model. To satisfy the heat flow constraint with average shear stress in the 10–20 MPa range, the fault zone friction coefficients must be 0.1–0.2 and < 0.05 in the conventional and extended models, respectively.

and gouge friction coefficient for values of $\bar{\tau}$ up to 100 MPa. The fault angle ψ according to equation (D2) is sensitive to the stress ratio r . For small angle ψ , it can be expressed as

$$\psi \approx \frac{1}{2} \frac{\sqrt{1 + \mu^2} + \mu}{r\mu} \left[\frac{\tau}{\sigma_V - p_o} \right] \quad (8)$$

[41] Since the quantities τ , σ_V and p_o all increase linearly with depth, the bracketed ratio is a constant and the fault angle ψ is proportional to $\bar{\tau}$ and inversely proportional to r . As illustrated in Figure 9b, if the stress ratio r is in the range 0.8–1.0 as inferred from SAFOD pilot hole data [Hickman and Zoback, 2004], then the angle ψ must be $<5^\circ$ to satisfy the heat flow constraint with $\bar{\tau} < 20$ MPa. In contrast, the effective normal stress is not sensitive to r or $\bar{\tau}$ (Figure 9c). Indeed it can be observed from equation (D3) that, for small angle ψ , the effective normal stress is simply given by

$$\sigma_n - p_f \approx \left(\frac{\sqrt{1 + \mu^2} + \mu}{\sqrt{1 + \mu^2} - \mu} \right) (\sigma_V - p_o) \quad (9a)$$

[42] In this scenario, the effective normal stress is directly proportional to the overburden minus hydrostatic pore pressure. The constant $\left(\frac{\sqrt{1 + \mu^2} + \mu}{\sqrt{1 + \mu^2} - \mu} \right)$ ranges from 3.12 to 4.68 for $\mu = 0.6$ –0.85, and therefore the normal stress is relatively large.

[43] According to (D4), the gouge friction coefficient is directly proportional to the average shear stress $\bar{\tau}$, but basically independent of the ratio r . For small angle ψ , it can be written as

$$\mu_f \approx \left(\frac{\sqrt{1 + \mu^2} - \mu}{\sqrt{1 + \mu^2} + \mu} \right) \frac{\tau}{(\sigma_V - p_o)} \quad (9b)$$

As illustrated in Figure 9d, the gouge friction coefficient must be very low ($\mu_f \approx 0.05$ or smaller) to satisfy the heat flow constraint with $\bar{\tau} < 20$ MPa. Such a value is much lower than the range of 0.1–0.2 often cited as necessary to satisfy the heat flow constraint (Figure 1b). This apparent discrepancy arises because we have followed Rice [1992] to impose the condition that the country rock is in the thrust faulting regime. In contrast, this problem is conventionally analyzed assuming the stress states in both the country rock and fault zone are in the strike-slip regime.

[44] We next consider this second scenario with the vertical stress corresponding to the intermediate principal stress. Since the normal stress in this regime is expected to fall somewhere between the maximum and minimum horizontal stresses, a plausible assumption is for the normal stress to be approximated by the vertical overburden [Morrow *et al.*, 1992, 1997; Moore and Rymer, 2007] and accordingly, we write the effective normal stress as

$$\sigma_n - p_f \approx (\sigma_V - p_o) \quad (10a)$$

and by definition, the gouge friction coefficient is given by

$$\mu_f = \frac{\tau}{(\sigma_n - p_f)} \approx \frac{\tau}{(\sigma_V - p_o)} \quad (10b)$$

Comparison of (10) with (9) shows that while the gouge friction coefficient in this second scenario is also proportional to the average shear stress $\bar{\tau}$, the normal stress required to satisfy the heat flow constraint is significantly

lower (Figure 9c). For the same reason, the friction coefficient required is higher in this scenario with the country rock assumed to be in the strike-slip regime, with a value in the range of 0.1–0.2 that is commonly cited.

[45] The SAFOD experiment has provided, and will continue to provide, new geophysical observations about the mechanics of faulting in the SAF system. Fault gouge material retrieved from 3 km depth in and adjacent to the active fault trace indicates the presence of weak clays, serpentinite and even talc. Laboratory tests of natural fault gouge sampled near the active San Andreas Fault trace show modest strength at room temperature, but Byerlee-type friction when heated above 280°C (~ 10 km depth). Chrysotile undergoes a similar strengthening with increasing temperature and pressure. This intrinsic moderate to high shear strength would require high pore fluid pressure within the fault zone to be consistent with heat flow and stress orientation constraints. Irwin and Barnes [1975] noted that in the vicinity of the creeping portion of the SAF, Franciscan metamorphic rock is found across the fault from crystalline Salinian complex and that this arrangement could lead to trapped fluids and superhydrostatic pore pressure in the fault zone. Yet direct measurements of pore pressure during SAFOD drilling showed only modest overpressure in the Franciscan and no indication of significant overpressure within the fault zone. If weak fault constraints are valid, then either pore pressure cannot be adequately measured with conventional techniques, or possibly the mechanisms that lead to overpressure become more effective deeper in the fault zone.

[46] Of all the potentially important fault zone materials that might be present at midcrustal depths, talc (and to a lesser degree brucite) is unusual in that it remains weak at elevated pressure-temperature conditions [Moore and Lockner, 2008]. Thus, significant amounts of talc (or small amounts located strategically within the fault zone) could result in low strength without appealing to elevated fluid pressure. Still, at present, only small quantities of talc have been observed at SAFOD. Furthermore, talc, like most low-strength sheet silicates, is likely to lead to fault creep rather than earthquakes. Since SAFOD is located at the transition between the locked and creeping sections of the SAF, it is possible that talc is responsible for low-stress creep where it is occurring in the San Andreas system.

[47] Other studies, especially focal plane inversions [see, e.g., Hardebeck and Michael, 2004], tend to find principal stress orientations in California intermediate between those predicted by either strong or weak fault models. Such an intermediate strength model becomes easier to reconcile with field and lab observations than either end-member model. Intrinsic strength of fault core material is typically lower than Byerlee-type friction due to the presence of weak alteration minerals [Lockner *et al.*, 2009, 2005]. To the degree that the intrinsic gouge strength is reduced [Lupini *et al.*, 1981; Logan and Rauenzahn, 1987; Morrow *et al.*, 1992; Brown *et al.*, 2003; Kopf and Brown, 2003; Crawford *et al.*, 2008; S. Tembe *et al.*, Effect of clay content and mineralogy on frictional sliding behavior of simulated gouges: Binary and ternary mixtures of quartz, illite and montmorillonite, submitted to *Journal of Geophysical Research*, 2009], the necessary fault zone pore pressure excess is also reduced. Ultimately, some combination of reduced intrinsic gouge strength, pore pressure excess and dynamic weakening mechanisms may all be operative. The relative importance of these properties and

mechanisms may be different at different localities along the fault as is suggested by the juxtaposition of locked and creeping fault segments within the SAF system.

5. Summary

[48] Elevated pore fluid pressure confined to the fault zone has long been hypothesized as the cause of weakening in the San Andreas Fault. An end-member conceptual model of this is the *Rice* [1992] model, where, even with large fault friction coefficient, pore pressure in the fault core could increase as needed, reducing the effective normal stress and therefore the fault strength. The adjoining crust is considered to be relatively strong, with limiting stresses comparable to those required to induce thrust faulting in a rock mass with Byerlee-type frictional strength. In this scenario a pronounced pore pressure excess can be generated and maintained within the fault gouge that would allow frictional sliding to occur at a low shear stress level, with a local stress state in the strike-slip regime and maximum principal stress oriented almost normal to the fault plane. In light of recent findings of weak clays, serpentine and talc phases in drill core and cuttings samples obtained from the SAFOD scientific borehole, we have extended the *Rice* [1992] model to include an intrinsically weak fault zone. This extension is fully consistent with the framework proposed by Rice.

[49] Values for the fault zone friction coefficient μ_f were obtained from published and newly acquired data from friction experiments conducted in the triaxial saw cut configuration at hydrothermal conditions (compatible with 0–15 km depth) on three materials: illite-bearing fault gouge from SAFOD ST1 3067 m MD core the serpentine mineral-chrysotile, and talc. Using only experimental values for μ_f , host rock friction of $\mu = 0.85$ and a directional constraint $\psi = 20^\circ$ (corresponding to σ_H making a 70° angle to the fault) in the model, the fault zone fluid pressure calculated by the model ranged from subhydrostatic to as much as 3 times σ_V and is sensitive to the relative magnitudes of the principal stresses (i.e., the magnitude of the intermediate principal stress σ_h in the host rock). It was found that incorporation of low friction materials in the model resulted in pore pressure and stress magnitudes less than those predicted using the original *Rice* [1992] model. Hydrostatic fault zone fluid pressures were possible for directional constraint $\psi = 20^\circ$ and host rock friction coefficients $\mu = 0.55$ to 0.85 if $\mu_f < 0.2$. Importantly though, in cases where hydrostatic fault zone pore pressure were viable, the shear stress exceeded the 10–20 MPa heat flow constraint.

[50] While the examples presented in this paper are for a weak SAF (near-fault-normal compression and low frictional heat production), the analytical relations can be applied to any transpressional strike-slip faulting regime, including higher fault strength and more oblique principal stress orientation. For cases where ψ increases, required fluid overpressure decreases but fault-parallel shear stress (and consequently frictional heating) increases. Analysis of the governing equations presented here has underscored the importance of determining the fault zone stress state and pore pressure. Unfortunately, for a transpressional faulting regime, this stress component is poorly constrained.

[51] Ultimately, the strength of the SAF may be intermediate between the end-member strong and weak fault

models. Natural fault gouges tend to contain weak alteration minerals and therefore have intrinsic strength below Byerlee-type friction. Thus, some combination of reduced friction coefficient, excess fault zone pore pressure and dynamic weakening processes could be operative in the SAF system. The specific laboratory results considered here may be most applicable to the creeping portion of the SAF, especially where the presence of talc or other weak mineral phases is a controlling factor. Additional scientific drilling projects, similar to SAFOD, probing locked portions of the fault may be necessary to fully understand the mechanics of damaging earthquakes along the San Andreas Fault system.

Appendix A: Fault Zone Stress State and Pore Pressure

[52] With reference to Figure 2, we derive here expressions for the stresses and pore pressure within the fault zone using Mohr circle analysis. Mechanical equilibrium at the interface between country rock and fault gouge necessarily requires the resolved shear and normal stress to be continuous across this interface [*Rice*, 1992]. Hence the stresses τ and σ_n can conveniently be derived using the Mohr circle for the horizontal principal stresses (σ_H , σ_h) in the country rock. Since the angle between σ_H and the fault normal (aligned with σ_n) is ψ , the resolved shear stress at the interface is

$$\tau = (1/2)(\sigma_H - \sigma_h) \sin 2\psi = (r/2)(\sigma_H - \sigma_V) \sin 2\psi \quad (A1)$$

where r is a principal stress ratio defined in equation (2). If the rock mass is pervaded by randomly distributed fractures and the pore pressure p_o as a function of depth is given by the hydrostatic gradient, then limiting values of σ_V and σ_H (for incipient failure of the rock mass) are related by equation (1), which we substitute in (A1) to arrive at

$$\tau = \frac{r\mu \sin 2\psi}{\sqrt{1 + \mu^2} - \mu} (\sigma_V - p_o) = \frac{r\mu \sin 2\psi}{\sqrt{1 + \mu^2} - \mu} (\rho_r - \rho_w)gz \quad (A2)$$

[53] Similarly we can derive the normal stress at the interface

$$\begin{aligned} \sigma_n &= \frac{1}{2}(\sigma_H + \sigma_h) + \frac{1}{2}(\sigma_H - \sigma_h) \cos 2\psi \\ &= p_o + \left[\frac{\sqrt{1 + \mu^2} + \mu - r\mu \sin^2 \psi}{\sqrt{1 + \mu^2} - \mu} \right] (\sigma_V - p_o) \\ &= p_o + \left[\frac{\sqrt{1 + \mu^2} + \mu - r\mu \sin^2 \psi}{\sqrt{1 + \mu^2} - \mu} \right] (\rho_r - \rho_w)gz \end{aligned} \quad (A3)$$

If the fault is critically stressed in the strike-slip regime, then the tangent with slope equal to the gouge friction coefficient μ_f should touch the gray Mohr circle in Figure 2, which represents the maximum and minimum principal stresses (σ_H^f , σ_h^f) inside the fault zone. With reference to this Mohr circle, it can readily be shown that the principal stresses are given by

$$\sigma_H^f = \sigma_n + \tau \left(\sqrt{1 + \mu^2} + \mu_f \right) \quad (A4)$$

$$\sigma_h^f = \sigma_n + \tau \left(\sqrt{1 + \mu^2} - \mu_f \right) \quad (A5)$$

The tangent should intersect the horizontal axis at a point corresponding to the local pore pressure p_f (Figure 2) within the fault. Furthermore, the frictional failure criterion would require the shear and normal stresses to be related by $\tau = \mu_f(\sigma_n - p_f)$, which implies

$$p_f = \sigma_n - \frac{\tau}{\mu_f} \quad (\text{A6})$$

Substituting (A2) and (A3) into (A4), we therefore obtain

$$\begin{aligned} \lambda &= \frac{p_f}{\sigma_v} = \frac{p_o}{\sigma_v} + \left[\frac{\sqrt{1 + \mu^2} + \mu - r\mu(\sin^2 \psi + \sin 2\psi/\mu_f)}{\sqrt{1 + \mu^2} - \mu} \right] \\ &\quad \cdot \left(1 - \frac{p_o}{\sigma_v} \right) \\ &= \frac{\rho_w}{\rho_r} + \left[\frac{\sqrt{1 + \mu^2} + \mu - r\mu(\sin^2 \psi + \sin 2\psi/\mu_f)}{\sqrt{1 + \mu^2} - \mu} \right] \left(1 - \frac{\rho_w}{\rho_r} \right) \end{aligned} \quad (\text{A7})$$

[54] The ratio λ is also called the Hubbert-Rubey coefficient. If the angle ψ is sufficiently small, then the term containing $\sin^2 \psi$ can be neglected and $\sin 2\psi$ can be approximated by 2ψ . Our computations show that for $\psi < 20^\circ$ or so, this turns out to be a good approximation for the range of friction coefficient we consider here. The Hubbert-Rubey coefficient can then be approximated by

$$\begin{aligned} \lambda &= \frac{p_f}{\sigma_v} \approx \frac{\rho_w}{\rho_r} + \left(\frac{\sqrt{1 + \mu^2} + \mu}{\sqrt{1 + \mu^2} - \mu} \right) \left(1 - \frac{\rho_w}{\rho_r} \right) \\ &\quad - \frac{2\mu}{\sqrt{1 + \mu^2} - \mu} \left(\frac{r\psi}{\mu_f} \right) \end{aligned} \quad (\text{A8})$$

Applying the same approximation to (A3), we obtain for the normal stress

$$\sigma_n \approx \sigma_H = p_o + \left[\frac{\sqrt{1 + \mu^2} + \mu}{\sqrt{1 + \mu^2} - \mu} \right] (\sigma_v - p_o) \quad (\text{A9})$$

and the effective normal stress

$$\sigma_n - p_f \approx \frac{2\mu}{\sqrt{1 + \mu^2} - \mu} \left(\frac{r\psi}{\mu_f} \right) (\sigma_v - p_o) \quad (\text{A10})$$

Appendix B: Frictional Strength of SAFOD Core Material at Elevated Temperatures and Pressures

B1. Description of SAFOD Gouge Material

[55] *Tembe et al.* [2006] have conducted a comprehensive investigation of the room temperature frictional strength of cuttings and spot core samples retrieved during SAFOD phases 1 and 2. They identified the weakest material to be from an illite clay layer ~ 30 cm thick in the spot core at measured depth (MD) of 3067 m. The black gouge (cut from 7 to 9 cm from the top of the core) had a friction

coefficient of 0.40–0.45 at room temperature. The shear zone is thought to be a minor inactive strand ~ 130 m southwest of the active SAF [*Hickman et al.*, 2005]. X-ray diffraction (XRD) analysis of *Solum et al.* [2006] determined composition of this gouge to be 48–51 weight % illite, 14–18% mixed illite-smectite, 19–22% feldspar, 11–17% quartz, 1% chlorite, and trace amounts of calcite. The mineralogy and texture were further studied by *Schleicher et al.* [2006] using scanning and transmission electron microscopy and XRD. They reported the presence of a natural, swelling smectite phase in the spot core from 3067 m MD and interpreted the slickenfiber geometries and related texture of this authigenic phase as mineral coatings on microfault surfaces associated with some increments of slip. Laboratory data have shown that the presence of clays in a gouge mixture can significantly lower the frictional strength [e.g., *Lupini et al.*, 1981; *Logan and Rauenzahn*, 1987; *Morrow et al.*, 1992; *Brown et al.*, 2003; *Kopf and Brown*, 2003; *Crawford et al.*, 2008; *Tembe et al.*, submitted manuscript, 2009]. However, most of the data were acquired at room temperature and to our knowledge, there have been no systematic investigations of the frictional properties of such gouge mixtures under hydrothermal conditions. Our experiments were conducted as a first step in characterizing the temperature dependence of natural fault gouge strength.

B2. Experimental Methodology

[56] The SAFOD 3067 m MD gouge was highly friable and contained many fractures incurred from previous tectonic episodes and during the coring process. Our best efforts to obtain intact specimens for mechanical testing were largely unsuccessful and it was ultimately decided to crush the material and test it as a simulated gouge. The powdered material was passed through a 100 mesh sieve to obtain particle sizes of $< 149 \mu\text{m}$ for experimental use. In the laboratory a geologic fault zone, consisting of a principal slip zone embedded in country rock, is represented by a thin gouge layer deformed between forcing blocks. Our high-temperature frictional sliding experiments were conducted in the conventional triaxial configuration on a 1 mm thick gouge layer sandwiched between Westerly granite forcing blocks. The forcing blocks were made from a single cylindrical sample of Westerly granite (1.91 cm in diameter and 4.06 cm in length) which was cut in half at a 30° incline. Although maximum displacement of the driving blocks is limited by the size of the pressure vessel, the triaxial apparatus allows for ambient pressures and displacement rates that are comparable to the tectonic stresses and creep rate of the SAF.

[57] The simulated gouge layer was first prepared as a thick paste with deionized water, which was spread onto the saw cut face of the upper forcing block, and then sandwiched by the lower block. The saw cut surfaces were roughened slightly with SiC powder to ensure coupling of the gouge layer and forcing blocks. To assure good pore pressure communication between the gouge layer and the external pore pressure system, the upper driving block contained a small hole drilled along the sample axis. The hole was then packed with medium-sized Ottawa sand to minimize extrusion of the gouge and allow the flow of fluids. The low porosity ($< 1\%$) of the lower granite driving block minimized water storage and pore pressure transients

that might be generated during rapid stress changes. Following the experimental procedure of Moore *et al.* [2004], the assembled saw cut sample was inserted into an annealed copper jacket between titanium carbide and Lucalox ceramic spacers and then slipped into a platinum resistance furnace. The space between the copper jacket and furnace was loosely packed with thermally conductive boron nitride and glass wool and then the entire assembly was placed in the pressure vessel.

[58] Confining pressure (argon gas medium) was applied first while the sample assembly and pore pressure lines were evacuated for 25 min. Deionized water was then introduced as the pore fluid and the sample allowed to equilibrate at pore pressure $p_f = 100$ MPa and confining pressure of 138–400 MPa. The confining pressure and pore pressure were computer controlled to within ± 0.3 MPa and ± 0.2 MPa, respectively.

[59] We assumed temperature was relatively well correlated with depth and chose run temperatures appropriate for 3–15 km depth. Based on heat flow for Central California (described in Appendix C), the corresponding run temperatures were 96–431°C. After pore pressure was raised to 100 MPa, temperature was increased gradually at a rate of $\sim 5^\circ\text{C}/\text{min}$ to the desired run value and the sample was allowed to equilibrate for 1 h.

[60] Axial loading was then applied to the saw cut sample such that the saturated gouge layer would be sheared under drained conditions (no internal rise in p_f within the gouge layer) at a fixed normal stress σ_n and constant pore pressure $p_f = 100$ MPa. Up to 3.5 mm of axial displacement (corresponding to 4.04 mm resolved on the inclined saw cut) would be reached in the experiments. A total of 12 experiments were performed at effective normal stresses $\sigma_n - p_f$ of 38–300 MPa and are summarized in Table 1. In each run a servo-controlled axial displacement rate of $0.5 \mu\text{m}/\text{s}$ was initially applied until an axial displacement of 1.5 mm had been attained. To measure the velocity-dependent response, the displacement rate was then alternated between 0.05 and $0.5 \mu\text{m}/\text{s}$ until the end of the run or until the jacket ruptured. Experimental displacement rates parallel to the saw cut correspond to 18.5 and 1.85 m/yr, compared with SAF creep rates of about 30 mm/yr [Titus *et al.*, 2006].

[61] The mechanical data were corrected for the elastic deformation of the loading system, jacket strength (details reported by Moore and Lockner [2008]), reduction in contact area between the sliding blocks during deformation, and confining pressure-dependent piston-seal friction, producing frictional shear strength values with estimated accuracy of ± 2 MPa. Since uncertainties in shear and normal stress are correlated in the triaxial geometry, uncertainties in the ratio $\mu = \tau/\sigma_n$ are estimated to be ± 0.01 when comparing values from different experiments. Changes in frictional strength during a single experiment, such as those due to displacement rate steps, will be more accurate since the measurements were made in the same run.

B3. Mechanical Data and Effect of Temperature

[62] The frictional strength data are presented in Figure B1 in terms of the coefficient of friction of the gouge $\mu_f = \tau/(\sigma_n - p_f)$, where τ and σ_n are shear and normal stress resolved on the saw cut surface and cohesion is assumed to equal zero. For each sample the friction coefficient values

attained at an axial displacement of 3.2 mm (corresponding to shear displacement of 3.7 mm resolved on the saw cut) are compiled in Table 1.

[63] Several features were observed in the frictional sliding data. First, the friction coefficient typically attained a relatively stable value at an axial displacement around 1 mm, beyond which strain hardening manifested by a slight increase in friction coefficient with axial displacement. It is important to consider that when slip in the experiments is limited to a few millimeters, the values of friction and velocity dependence may not represent a true steady state, but reflect an evolving system. This may be apparent in the mechanical data as a strain-hardening/softening trend due to ongoing cataclasis, compaction, and strain localization within the gouge layer as well as time-dependent fluid-rock interactions if the gouge is chemically out of equilibrium. In our experiments the effect was most pronounced at high temperatures. For runs that terminated early the friction coefficient values reported in Table 1 were extrapolated to 3.2 mm by assuming a linear strain hardening trend for an axial displacement rate of $0.5 \mu\text{m}/\text{s}$.

[64] Second, while experiments conducted at the same temperature demonstrate pressure dependence, the temperature dependence is far greater, with values ranging from 0.4 at 96°C , comparable to the room temperature findings (Figure B1), up to 0.73 at 431°C . Similar dependence has been observed in heated chrysotile [Moore *et al.*, 2004]. Third, each velocity step was associated with a transient perturbation in the friction coefficient in the same sense as the velocity step. Stick-slip behavior accompanied velocity step changes in the run at 300 MPa (Figure B1c) and oscillatory behavior was observed at 283°C (Figure B1b) and at 150 MPa (Figure B1c). Smaller-amplitude-high-frequency noise in the mechanical data is due to $<3^\circ\text{C}$ fluctuations in the temperature.

B4. Friction Coefficient as a Function of Depth Constrained by Laboratory Data

[65] In this section, we describe the procedure for constructing the friction versus depth profiles presented in Figure 4. The first step involves mapping temperature into depth using the appropriate geotherm for the San Andreas Fault at SAFOD. This calculation is provided in Appendix C. Next, we use laboratory data, such as that presented in Table 1, that relate friction coefficient to temperature and effective normal stress. Talc friction as reported by Moore and Lockner [2007, 2008] shows little sensitivity to either temperature or normal stress and was interpolated directly as shown in Figures 4 and 7a. The strength of chrysotile and to a lesser degree, SAFOD black gouge, was sensitive to effective normal stress at constant temperature. The stress-temperature sensitivity of SAFOD black gouge is apparent in Table 1. The problem becomes, as shown in Figure B2a, finding the coefficient of friction for the gouge material (at a given temperature) that simultaneously matches the experimental data and the model solution given by (4) and (5). Experimental data are approximated by a linear trend (dashed line in the example in Figure B2a) relating friction to effective normal stress. The model fit for $z = 9$ km, $\mu = 0.85$, $r = 0.5$ and $\psi = 20^\circ$ becomes the locus of points plotted as the solid curved line in Figure B2a. The unique values of μ_f and effective normal stress that satisfy both the model and the

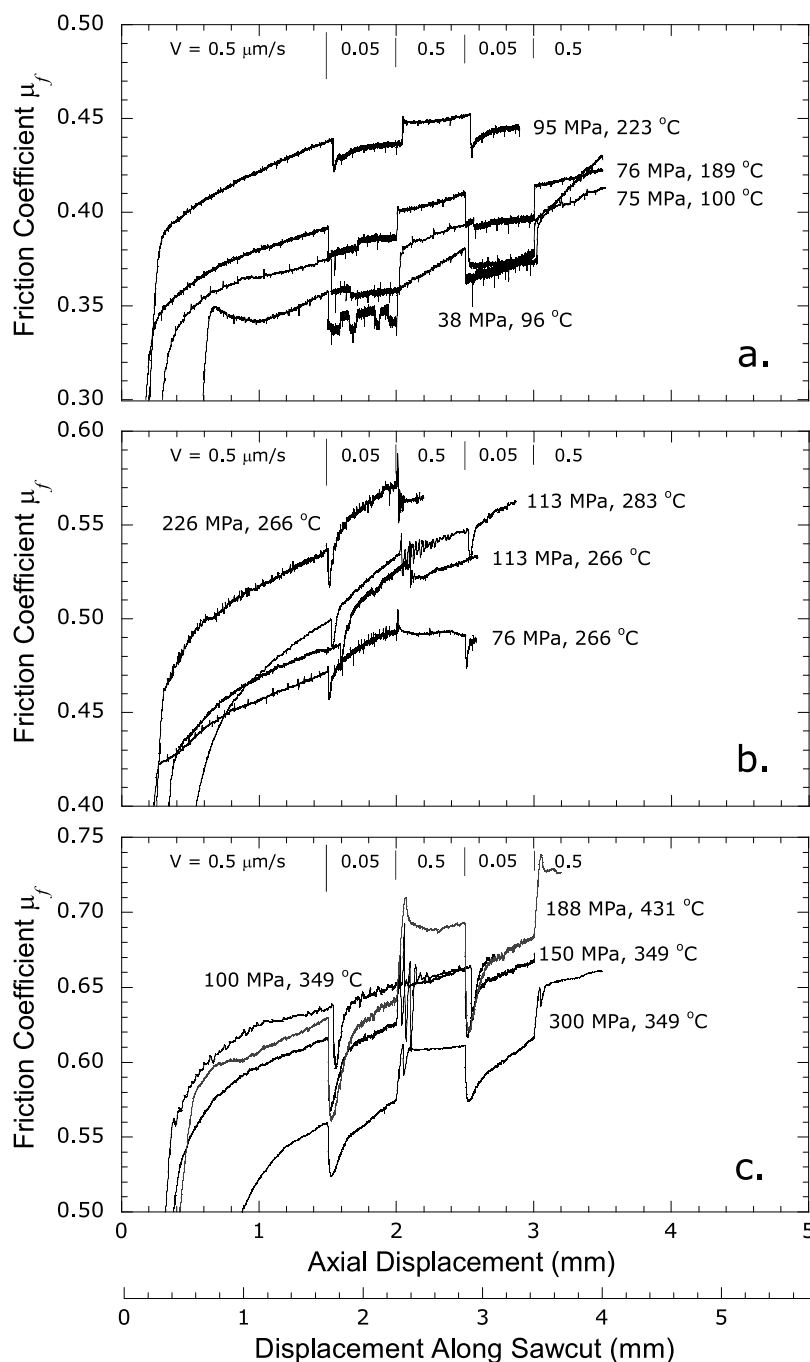


Figure B1. Friction coefficient-displacement curves for experimental runs on the black gouge at the indicated effective normal stress ($\sigma_n - p_f$) and temperature. The maximum axial displacement reached was 3.5 mm (corresponding to 4.04 mm resolved on the saw cut) at alternating axial displacement rates of 0.5 and 0.05 $\mu\text{m/s}$. The frictional sliding behavior can be characterized by three regimes at (a) low temperature ($T < 266^\circ\text{C}$) with velocity-strengthening behavior, (b) intermediate temperature ($266^\circ\text{C} \leq T \leq 283^\circ\text{C}$) with velocity weakening, and (c) high temperature ($T > 283^\circ\text{C}$) with velocity-strengthening behavior.

experimental data are represented graphically by the intersection of the two lines. Friction coefficients so inferred for the SAFOD black gouge are plotted as a function of depth for three different values of r in Figure B2b. In cases where only one measurement of friction coefficient was made at a given temperature, we assumed no dependence on the effective normal stress. The friction coefficient of the black

gouge was found to increase appreciably at depths below 6 km, attaining peak values of 0.68–0.79 at 15 km. Because chrysotile strength is significantly more sensitive to normal stress than the SAFOD black gouge, strength profiles of chrysotile as plotted in Figures 4 and 6a show the greatest variation.

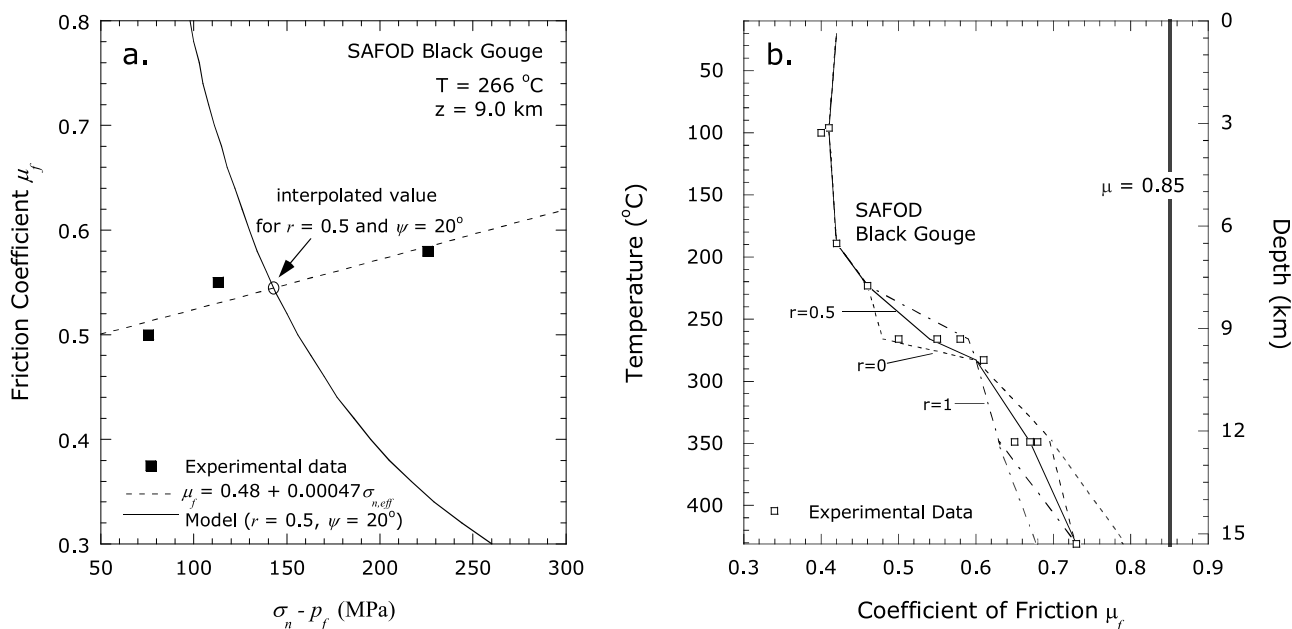


Figure B2. (a) Interpolation of coefficient of friction from data for multiple experimental runs at a single temperature. The example depicted is for $T = 266^\circ\text{C}$ (corresponding to $z = 9\text{ km}$), $r = 0.5$, and $\psi = 20^\circ$. The experimental data at 266°C and three different effective normal stresses were fitted to provide a linear relation between friction coefficient and effective normal stress. The solid line is the effective normal stress (for $z = 9\text{ km}$, $r = 0.5$ and $\psi = 20^\circ$) as a function of the gouge friction coefficient according to equations (4) and (5). The point where the solid curve intersects the dashed line corresponds to the optimal friction coefficient for the depth and parameters considered. This approach can only be applied when the normal stress dependence is sufficiently constrained by multiple experimental data points. (b) The coefficient of friction μ_f as a function of temperature and depth for the SAFOD Black Gouge. We plot the temperature dependence of friction for three stress ratios ($r = 0, 0.5$, and 1) inferred from laboratory data using the approach summarized in Appendix B and outlined in Figure B2a. The geothermal regime can be approximated by a linear gradient of $\sim 28^\circ\text{C}/\text{km}$ (Appendix C), which was used to relate temperature to depth. The dashed gray lines between 12 and 15 km represent the trajectories of $r = 0$ and $r = 1$. Since only one experiment was conducted at this temperature-depth, the friction coefficient is unconstrained.

B5. Rate Sensitivity and Velocity Weakening in the SAFOD Gouge

[66] The response of steady state frictional sliding to velocity perturbations can be characterized by the quantity $d\mu_{ss}/d \ln V$, where μ_{ss} denotes the steady state coefficient of friction at the slip velocity V . In the context of the rate- and state-dependent friction model [Dieterich, 1979], this quantity is given by the difference $a - b$, with a and b characterizing the “direct” and “evolution” effects in response to perturbations in slip velocity [Paterson and Wong, 2005]. Positive and negative values of $a - b = d\mu_{ss}/d \ln V$ thus correspond to velocity strengthening and weakening, respectively. The SAFOD black gouge experimental data naturally fall into three thermomechanical regimes: low-temperature ($T < 266^\circ\text{C}$) with velocity-strengthening behavior, intermediate-temperature ($266^\circ\text{C} \leq T \leq 283^\circ\text{C}$) with velocity-weakening behavior, and high temperature with predominantly velocity strengthening.

[67] In each experiment we made several changes in the loading velocity (Figure B1) and the velocity dependence was then quantified from the corresponding changes in friction coefficient. In Figure B3 we plot velocity dependence of the friction coefficient ($a - b$)

as a function of temperature and equivalent depth. The uncertainty in these estimates is typically around ± 0.0004 . Values for $a - b$ range from -0.0056 up to $+0.0115$ with negative values occurring in the intermediate regime and positive values in the low- and high-temperature regimes. The most interesting of these is the intermediate regime, which covers a temperature range corresponding to $9.0\text{--}9.6\text{ km}$ depth and exhibits transient frictional behavior relevant to seismogenesis.

[68] At least three factors may contribute to velocity-weakening behavior in the SAFOD gouge experiments in the temperature interval $266\text{--}283^\circ\text{C}$. First, the velocity step intervals may be too short to achieve steady state, giving the impression of negative $a - b$ values. Second, while constant pore pressure was maintained in the pore pressure system during the experiment, it was assumed that the migration of water in or out of the gouge layer occurs at a rate that keeps up with volumetric changes induced by shearing of the layer. Although we used slow displacement rates to enable a fully drained gouge (velocity steps alternated between 1,000 and 10,000 s), in a low-permeability clay material it may be possible to trap fluids and, if the gouge compacts, raise the pore pressure locally and reduce the effective stress. There was, however, no indication in the

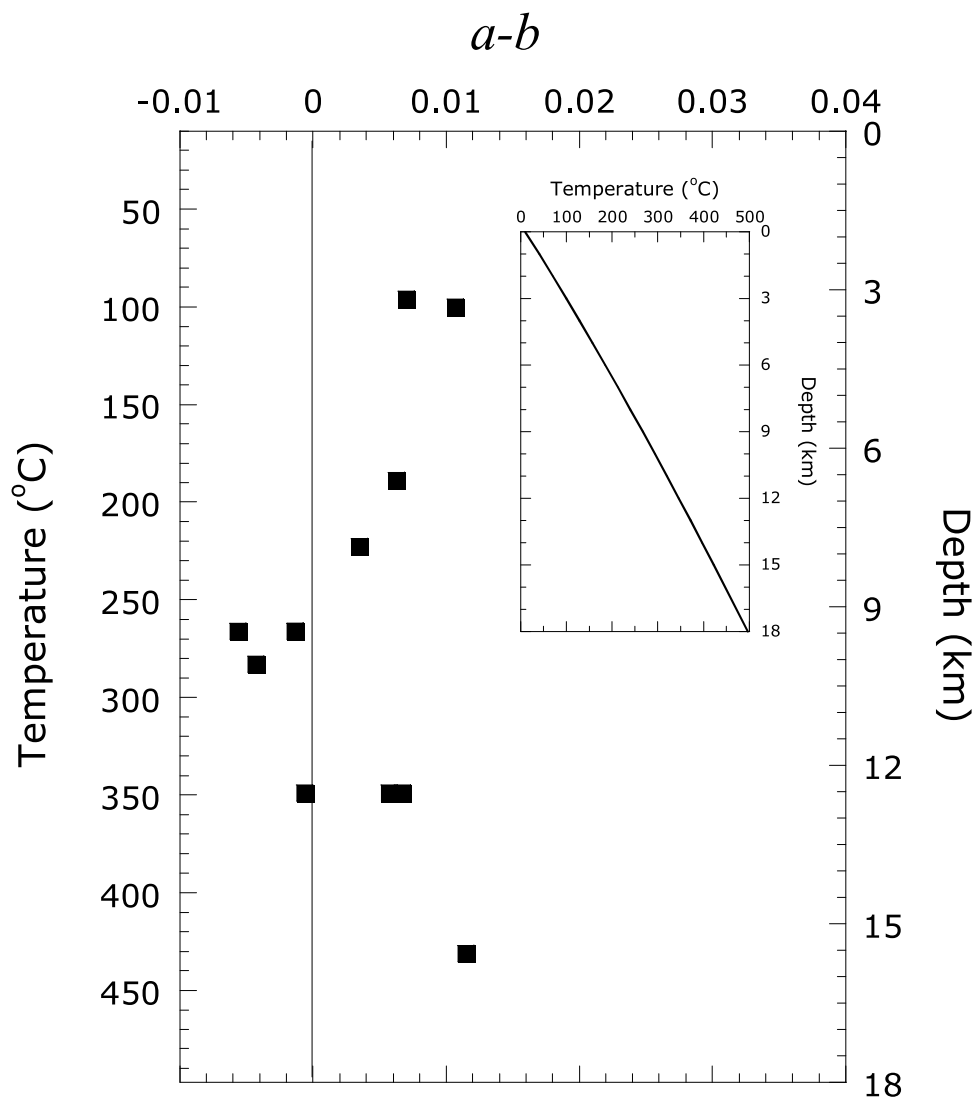


Figure B3. Velocity dependence of steady state friction for the SAFOD 3067 m MD black gouge as functions of temperature and depth. Measurement uncertainty is roughly equal to symbol size. The inset shows the correspondence between temperature and depth for the Parkfield region (see Appendix C for details).

mechanical data that this problem occurred. Third, the narrow temperature range over which velocity weakening was observed would suggest a chemical origin such as a phase change (for example, smectite to illite) or a dehydration reaction, which would lubricate the grains during sliding. As we mentioned, this set of experiments was intended to be exploratory in nature and further detailed tests are warranted.

[69] To determine whether the velocity weakening was due to a phase change, we must identify the minerals involved in the reaction and determine the reaction temperature and kinetics at pressures relevant to our experimental conditions. The major mineral constituents of the SAFOD gouge are illite, smectite, quartz, and feldspar and previous studies have found a correlation between temperature and the onset of unstable sliding in all these materials. *Moore et al.* [1989] noted stick-slip behavior in illite at temperatures above 400°C. Studies on wet granite [e.g., *Stesky*, 1978; *Blanpied et al.*, 1991] and quartz [e.g., *Higgs*, 1981; *Chester*

and *Higgs*, 1992] also show weakening at elevated temperatures and comparable sliding rates, but the temperatures involved are typically much greater. In contrast, smectite is known to dehydrate at relatively low temperatures and experimental data by *Logan et al.* [1981] on nominally montmorillonite-rich gouge showed stick-slip behavior at 300°C. Dehydration may be related to the illitization of smectite around 150°C. This reaction requires a complex rearrangement of atoms that may be sluggish when compared to the duration of our experiments. However, paucity of data at in situ conditions, uncertainty in the reaction process, and the need for detailed microscopy of our samples leaves this an open question.

Appendix C: Geothermal Gradient at Parkfield

[70] To infer the frictional strength at seismogenic depths from our hydrothermal friction data for the SAFOD gouge, we must first specify a geothermal gradient for the SAF. A

comprehensive study of the thermal regime of the SAF near Parkfield was conducted by *Sass et al.* [1997], who adopted the following relation of *Lachenbruch and Sass* [1977] to extrapolate their heat flow data to temperature T as a function of depth z

$$\theta(z) = T(z) - T_s = \frac{1}{\lambda} \left[(q - DA_o)z + D^2 A_o (1 - e^{-z/D}) \right] \quad (C1)$$

The derivation of this relation assumes that radiogenic heat production decays exponentially over depth, with a characteristic decay depth of $D = 15$ km. Here we use a value of $A_o = 1.5 \mu\text{Wm}^{-3}$ for heat production as suggested by *Sass et al.* [1997]. For the surface heat flow and thermal conductivity λ we use updated values of $q = 77 \text{ mWm}^{-2}$ and $\lambda = 2.5 \text{ Wm}^{-1} \text{ K}^{-1}$ reported by *Williams et al.* [2004] and *Williams* [1996], respectively. We also assign a surface temperature of $T_s = 10^\circ\text{C}$. The geotherm is almost linear with a gradient approximately equal to 28°C/km .

Appendix D: Imposing the Heat Flow Constraint

[71] The shear stress is assumed to increase linearly with depth in a seismogenic layer of thickness L :

$$\tau = 2\bar{\tau} \frac{z}{L} \quad (D1)$$

With reference to the Mohr circle associated with principal stresses σ_h and σ_H (Figure 2), we can use equation (A2) to derive the stress orientation:

$$\begin{aligned} \psi &= \frac{1}{2} \sin^{-1} \left(\frac{\tau}{(\sigma_V - p_o)} \frac{(\sqrt{1 + \mu^2} - \mu)}{r\mu} \right) \\ &= \frac{1}{2} \sin^{-1} \left(\frac{2\bar{\tau}}{(\rho_r - \rho_w)gL} \frac{(\sqrt{1 + \mu^2} - \mu)}{r\mu} \right) \end{aligned} \quad (D2)$$

The pore pressures in the country rock and fault zone are both assumed to be hydrostatic. Hence, we can substitute into (A3) to calculate the effective normal stress:

$$\begin{aligned} \sigma_n - p_f &= \sigma_n - p_o = \left(\frac{\sqrt{1 + \mu^2} + \mu - r\mu \sin^2 \psi}{\sqrt{1 + \mu^2} - \mu} \right) (\sigma_V - p_o) \\ &= \left(\frac{\sqrt{1 + \mu^2} + \mu - r\mu \sin^2 \psi}{\sqrt{1 + \mu^2} - \mu} \right) (\rho_r - \rho_w)gz \end{aligned} \quad (D3)$$

The gouge friction coefficient that is compatible with such a shear stress profile can then be determined either by substituting (D3) into the relation $\mu_f = \tau/(\sigma_n - p_o)$, or by imposing the condition $p_f = p_o$ in (5):

$$\begin{aligned} \mu_f &= \left(\frac{\sqrt{1 + \mu^2} - \mu}{\sqrt{1 + \mu^2} + \mu - r\mu \sin^2 \psi} \right) \frac{\tau}{(\sigma_V - p_o)} \\ &= \left(\frac{\sqrt{1 + \mu^2} - \mu}{\sqrt{1 + \mu^2} + \mu - r\mu \sin^2 \psi} \right) \frac{2\bar{\tau}}{(\rho_r - \rho_w)gL} \end{aligned} \quad (D4)$$

[72] **Acknowledgments.** We thank D. J. Andrews, D. Faulkner, E. Rutter, and C. Scholz for their thoughtful comments. We have benefited from discussions with them and Stephen Hickman, Diane Moore, Carolyn Morrow, and Colin Williams. Sheryl Tembe was supported by a DOEEd GAANN fellowship. This research was partially supported by U.S. National Science Foundation under grant EAR-0346022.

References

- Anderson, E. M. (1951), *The Dynamics of Faulting and Dyke Formation With Application to Britain*, Oliver and Boyd, White Plains, N. Y.
- Andrews, D. J. (2002), A fault constitutive relation accounting for thermal pressurization of pore fluid, *J. Geophys. Res.*, *107*(B12), 2363, doi:10.1029/2002JB001942.
- Blanpied, M. L., D. A. Lockner, and J. D. Byerlee (1991), Fault stability inferred from granite sliding experiments at hydrothermal conditions, *Geophys. Res. Lett.*, *18*, 609–612, doi:10.1029/91GL00469.
- Boness, N. L., and M. D. Zoback (2006), A multiscale study of the mechanisms controlling shear velocity anisotropy in the San Andreas Fault Observatory at Depth, *Geophysics*, *71*(5), F131–F136, doi:10.1190/1.2231107.
- Brace, W. F., and D. L. Kohlstedt (1980), Limits on lithospheric stress imposed by laboratory experiments, *J. Geophys. Res.*, *85*, 6248–6252, doi:10.1029/JB085iB11p06248.
- Brown, K. M., A. Kopf, M. B. Underwood, and J. L. Weinberger (2003), Compositional and fluid pressure controls on the state of stress on the Nankai subduction thrust: A weak plate boundary, *Earth Planet. Sci. Lett.*, *214*, 589–603, doi:10.1016/S0012-821X(03)00388-1.
- Brune, J. N., T. Henyey, and R. Roy (1969), Heat flow, stress, and rate of slip along San Andreas Fault, California, *J. Geophys. Res.*, *74*, 3821–3827, doi:10.1029/JB074i015p03821.
- Byerlee, J. D. (1978), Friction of rocks, *Pure Appl. Geophys.*, *116*, 615–626, doi:10.1007/BF00876528.
- Byerlee, J. D. (1990), Friction, overpressure, and fault normal compression, *Geophys. Res. Lett.*, *17*, 2109–2112, doi:10.1029/GL017i012p02109.
- Byerlee, J. D. (1992), The change in orientation of subsidiary shears near faults containing pore fluid under high pressure, *Tectonophysics*, *211*, 295–303, doi:10.1016/0040-1951(92)90066-F.
- Byerlee, J. D., and J. C. Savage (1992), Coulomb plasticity within the fault zone, *Geophys. Res. Lett.*, *19*, 2341–2344, doi:10.1029/92GL02370.
- Chéry, J., M. D. Zoback, and S. Hickman (2004), A mechanical model of the San Andreas Fault and SAFOD Pilot Hole stress measurements, *Geophys. Res. Lett.*, *31*, L15S13, doi:10.1029/2004GL019521.
- Chester, F. M., and N. G. Higgs (1992), Multimechanism friction constitutive model for ultrafine quartz gouge at hypocentral conditions, *J. Geophys. Res.*, *97*, 1859–1870, doi:10.1029/91JB02349.
- Crawford, B. R., D. R. Faulkner, and E. H. Rutter (2008), Strength, porosity, and permeability development during hydrostatic and shear loading of synthetic quartz-clay fault gouge, *J. Geophys. Res.*, *113*, B03207, doi:10.1029/2006JB004634.
- Dieterich, J. H. (1979), Modeling of rock friction: 1. Experimental results and constitutive equations, *J. Geophys. Res.*, *84*, 2161–2168, doi:10.1029/JB084iB05p02161.
- Escartin, J., M. Andreani, G. Hirth, and B. Evans (2008), Relationships between the microstructural evolution and the rheology of talc at elevated pressures and temperatures, *Earth Planet. Sci. Lett.*, *268*(3–4), 463–475, doi:10.1016/j.epsl.2008.02.004.
- Faulkner, D. R., T. M. Mitchell, D. Healy, and M. J. Heap (2006), Slip on ‘weak’ faults by the rotation of regional stress in the fracture damage zone, *Nature*, *444*, 922–925, doi:10.1038/nature05353.
- Hardebeck, J. L., and A. J. Michael (2004), Stress orientations at intermediate angles to the San Andreas Fault, California, *J. Geophys. Res.*, *109*, B11303, doi:10.1029/2004JB003239.
- Hickman, S., and M. D. Zoback (2004), Stress orientations and magnitudes in the SAFOD pilot hole, *Geophys. Res. Lett.*, *31*, L15S12, doi:10.1029/2004GL020043.
- Hickman, S. H., M. D. Zoback, and W. L. Ellsworth (2005), Structure and composition of the San Andreas Fault Zone at Parkfield: Initial results from SAFOD phases 1 and 2, *Eos Trans. AGU*, *86*(52), Fall Meet. Suppl., Abstract T23E-05.
- Higgs, N. G. (1981), Mechanical properties of ultrafine quartz, chlorite and bentonite in environments appropriate to upper-crustal earthquakes, Ph.D. dissertation, Tex. A&M. College Station.
- Irwin, W. P., and I. Barnes (1975), Effect of geologic structure and metamorphic fluids on seismic behavior of the San Andreas Fault system in central and northern California, *Geology*, *3*, 713–716, doi:10.1130/0091-7613(1975)3<713:E0GSAM>2.0.CO;2.
- Kopf, A., and K. M. Brown (2003), Friction experiments on saturated sediments and their implications for the stress state of the Nankai and Barbados subduction thrust, *Mar. Geol.*, *202*(3–4), 193–210, doi:10.1016/S0025-3227(03)00286-X.

- Lachenbruch, A., and J. Sass (1977), Heat flow in the United States and the thermal regime of the crust, in *The Earth's Crust: Its Nature and Physical Properties*, *Geophys. Monogr. Ser.*, vol. 20, edited by J. G. Heacock, pp. 626–675, AGU, Washington, D. C.
- Lachenbruch, A., and J. Sass (1980), Heat flow and energetics of the San Andreas Fault zone, *J. Geophys. Res.*, *85*, 6185–6222, doi:10.1029/JB085iB11p06185.
- Lachenbruch, A., and J. Sass (1992), Heat flow from Cajon Pass, fault strength, and tectonic implications, *J. Geophys. Res.*, *97*, 4995–5015, doi:10.1029/91JB01506.
- Lockner, D. A., and N. M. Beeler (2002), Rock failure and earthquakes, in *International Handbook of Earthquake and Engineering Seismology*, edited by W. H. K. Lee, H. Kanamori, P. C. Jennings, and C. Kisslinger, pp. 505–537, Academic, Amsterdam.
- Lockner, D. A., C. Morrow, S.-R. Song, S. Tembe, and T.-f. Wong (2005), Permeability of whole core samples of Chelungpu fault, Taiwan TCDP scientific drillhole, *Eos Trans. AGU*, *86*(52), Fall Meet. Suppl., Abstract T43D-04.
- Lockner, D. A., H. Tanaka, H. Ito, R. Ikeda, K. Omura, and H. Naka (2009), Geometry of the Nojima fault at Nojima-Hirabayashi, Japan - I. A simple damage structure inferred from borehole core permeability, *Pure Appl. Geophys.*, *166*, 1649–1667, doi:10.1007/s00024-009-0515-0.
- Logan, J. M., and K. A. Rauenzahn (1987), Frictional dependence of gouge mixtures of quartz and montmorillonite on velocity, composition and fabric, *Tectonophysics*, *144*, 87–108, doi:10.1016/0040-1951(87)90010-2.
- Logan, J. M., N. Higgs, and M. Friedman (1981), Laboratory studies of natural fault gouge from the USGS No. 1 well in the San Andreas Fault zone, in *Mechanical behavior of Crystal Rocks: The Handin Volume*, *Geophys. Monogr. Ser.*, vol. 24, edited by N. L. Carter et al., pp. 121–134, AGU, Washington, D. C.
- Lupini, J. F., A. E. Skinner, and P. R. Vaughan (1981), The drained residual strength of cohesive soils, *Geotechnique*, *31*(2), 181–213.
- Moore, D. E., and D. A. Lockner (2007), Comparative deformation behavior of minerals in serpentinized ultramafic rock: Application to the slab-mantle interface in subduction zones, *Int. Geol. Rev.*, *49*, 401–415, doi:10.2747/0020-6814.49.5.401.
- Moore, D. E., and D. A. Lockner (2008), Talc friction in the temperature range 25°–400°C: Relevance for fault-zone weakening, *Tectonophysics*, *449*, 120–132, doi:10.1016/j.tecto.2007.11.039.
- Moore, D. E., and M. J. Rymer (2007), Talc-bearing serpentinite and the creeping section of the San Andreas Fault, *Nature*, *448*, 795–797, doi:10.1038/nature06064.
- Moore, D. E., R. Summers, and J. D. Byerlee (1989), Sliding behavior and deformation textures of heated illite gouge, *J. Struct. Geol.*, *11*(3), 329–342, doi:10.1016/0191-8141(89)90072-2.
- Moore, D. E., D. A. Lockner, R. Summers, S. Ma, and J. D. Byerlee (1996), Strength of chrysotile-serpentinite gouge under hydrothermal conditions: Can it explain a weak San Andreas Fault?, *Geology*, *24*(11), 1041–1045, doi:10.1130/0091-7613(1996)024<1041:SOCSGU>2.3.CO;2.
- Moore, D. E., D. A. Lockner, R. Summers, S. Ma, and J. D. Byerlee (1997), Strengths of serpentinite gouges at elevated temperatures, *J. Geophys. Res.*, *102*, 14,787–14,801, doi:10.1029/97JB00995.
- Moore, D. E., D. A. Lockner, H. Tanaka, and K. Iwata (2004), The coefficient of friction of chrysotile gouge at seismogenic depths, *Int. Geol. Rev.*, *46*, 385–398, doi:10.2747/0020-6814.46.5.385.
- Morrow, C. A., B. Radney, and J. D. Byerlee (1992), Frictional strength and the effective pressure law of montmorillonite and illite clays, in *Fault Mechanics and Transport Properties of Rocks*, edited by B. Evans and T.-f. Wong, pp. 69–88, Academic, San Diego, Calif.
- Morrow, C. A., D. E. Moore, and D. A. Lockner (2001), Permeability reduction in granite under hydrothermal conditions, *J. Geophys. Res.*, *106*, 30,551–30,560, doi:10.1029/2000JB000010.
- Morrow, C., J. G. Solum, S. Tembe, D. A. Lockner, and T.-f. Wong (2007), Using drill cutting separates to estimate the strength of narrow shear zones at SAFOD, *Geophys. Res. Lett.*, *34*, L11301, doi:10.1029/2007GL029665.
- Mount, V. S., and J. Suppe (1987), State of stress near San Andreas Fault: Implications for wrench tectonics, *Geology*, *15*, 1143–1146, doi:10.1130/0091-7613(1987)15<1143:SOSNTS>2.0.CO;2.
- Paterson, M. S., and T.-f. Wong (2005), Friction and sliding phenomena, in *Experimental Deformation—The Brittle Field*, pp. 165–210, Springer, New York.
- Reinen, L. A., J. D. Weeks, and T. E. Tullis (1991), The frictional behavior of serpentinite: Implications for aseismic creep on shallow crustal faults, *Geophys. Res. Lett.*, *18*, 1921–1924, doi:10.1029/91GL02367.
- Reinen, L. A., J. D. Weeks, and T. E. Tullis (1994), The frictional behavior of lizardite and antigorite serpentinites: Experiments, constitutive models, and implications for natural faults, *Pure Appl. Geophys.*, *143*, 317–358, doi:10.1007/BF00874334.
- Rice, J. R. (1992), Fault stress states, pore pressure distributions, and the weakness of the San Andreas Fault, in *Fault Mechanics and Transport Properties of Rocks*, edited by B. Evans and T.-f. Wong, pp. 475–504, Academic, San Diego, Calif.
- Rutter, E. H., and R. H. Maddock (1992), On the mechanical properties of synthetic kaolinite/quartz fault gouge, *Terra Nova*, *4*, 489–500, doi:10.1111/j.1365-3121.1992.tb00585.x.
- Sass, J. H., C. F. Williams, A. H. Lachenbruch, S. P. Galanis Jr., and F. V. Grubb (1997), Thermal regime of the San Andreas fault near Parkfield, California, *J. Geophys. Res.*, *102*, 27,575–27,585, 10.1029/JB102iB12p27575.
- Schleicher, A. M., B. A. van der Pluijm, J. G. Solum, and L. N. Warr (2006), Origin and significance of clay-coated fractures in mudrock fragments of the SAFOD borehole (Parkfield, California), *Geophys. Res. Lett.*, *33*, L16313, doi:10.1029/2006GL026505.
- Scholz, C. H. (2000), Evidence for a strong San Andreas Fault, *Geology*, *28*, 163–166, doi:10.1130/0091-7613(2000)28<163:EFASSA>2.0.CO;2.
- Scholz, C. H., and T. C. Hanks (2004), The strength of the San Andreas Fault: A discussion, in *Rheology and Deformation of the Lithosphere at Continental Margins*, edited by G. D. Karner et al., pp. 261–283, Columbia Univ. Press, New York.
- Sibson, R. H. (1990), Conditions for fault-valve behavior, in *Deformation Mechanisms, Rheology and Tectonics*, edited by R. J. Knipe and E. H. Rutter, *Geol. Soc. Spec. Publ.*, *54*, 15–28.
- Sleep, N. H., and M. L. Blanpied (1992), Creep, compaction and the weak rheology of major faults, *Nature*, *359*, 687–692, doi:10.1038/359687a0.
- Solum, J. G., S. H. Hickman, D. A. Lockner, D. E. Moore, B. A. van der Pluijm, and J. P. Evans (2006), Mineralogical characterization of protholith and fault rocks from the SAFOD main hole, *Geophys. Res. Lett.*, *33*, L21314, doi:10.1029/2006GL027285.
- Solum, J. G., et al. (2007), San Andreas Fault Zone mineralogy, geochemistry, and physical properties from SAFOD cuttings and core, *Sci. Drill.*, special issue, *1*(3), 64–67, doi:10.2204/iodp.sd.s01.34.2007.
- Stesky, R. M. (1978), Mechanisms of high temperature frictional sliding in Westerly granite, *Can. J. Earth Sci.*, *15*, 361–375, doi:10.1139/e78-042.
- Tembe, S., D. A. Lockner, J. G. Solum, C. A. Morrow, T.-f. Wong, and D. E. Moore (2006), Frictional strength of cuttings and core from SAFOD drillhole phases 1 and 2, *Geophys. Res. Lett.*, *33*, L23307, doi:10.1029/2006GL027626.
- Titus, S. J., C. DeMets, and B. Tikoff (2006), Thirty-five-year creep rates for the creeping segment of the San Andreas Fault and the effects of the 2004 M 6.0 Parkfield earthquake: Constraints from alignment arrays, continuous GPS, and creepmeters, *Bull. Seismol. Soc. Am.*, *96*, S250–S268, doi:10.1785/0120050811.
- Wiersberg, T., and J. Erzinger (2007), A helium isotope cross-section study through the San Andreas Fault at seismogenic depths, *Geochem. Geophys. Geosyst.*, *8*(1), Q01002, doi:10.1029/2006GC001388.
- Williams, C. (1996), Temperature and the seismic/aseismic transition: Observations from the 1992 Landers earthquake, *Geophys. Res. Lett.*, *23*, 2029–2032, doi:10.1029/96GL020666.
- Williams, C., F. V. Grubb, and S. P. Galanis (2004), Heat flow in the SAFOD pilot hole and implications for the strength of the San Andreas Fault, *Geophys. Res. Lett.*, *31*, L15S14, doi:10.1029/2003GL019352.
- Zoback, M. D. (2000), Strength of the San Andreas, *Nature*, *405*, 31–32, doi:10.1038/35011181.
- Zoback, M. D., et al. (1987), New evidence for the state of stress on the San Andreas Fault system, *Science*, *238*, 1105–1111, doi:10.1126/science.238.4830.1105.

D. Lockner, Earthquake Hazards Team, U.S. Geological Survey, MS 977, 345 Middlefield Road, Menlo Park, CA 94025, USA.

S. Tembe, Institute for Soil Mechanics and Rock Mechanics, Karlsruhe Institute of Technology, D-76128 Karlsruhe, Germany. (sheryl.tembe@kit.edu)

T.-f. Wong, Department of Geosciences, State University of New York at Stony Brook, ESS Building, Stony Brook, NY 11794-2100, USA.